Volume 7 | Number 20 | 21 October 2023

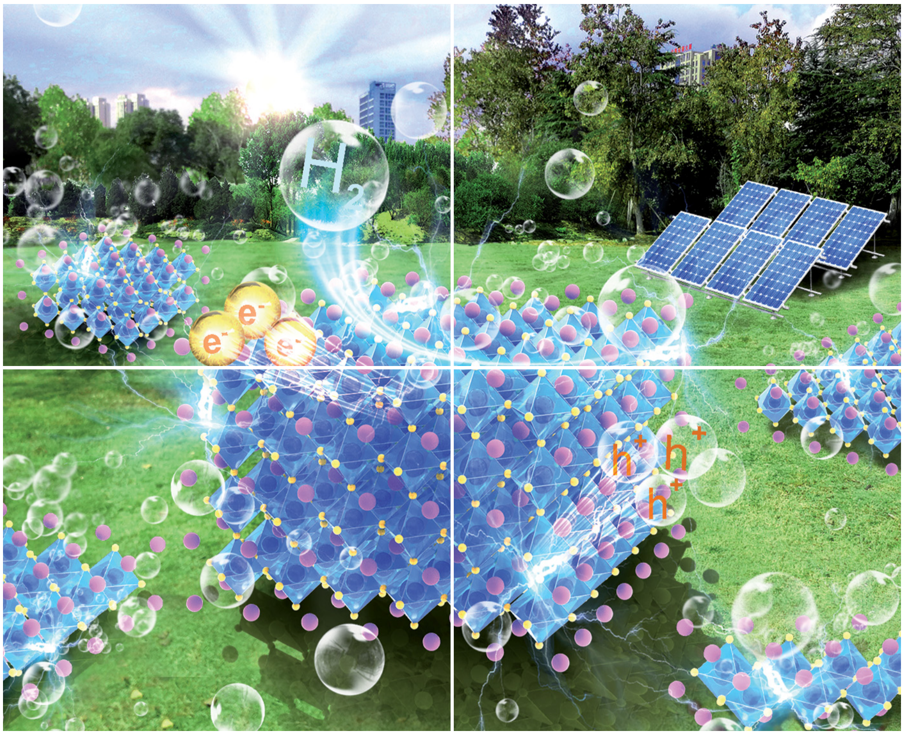

MATERIALS CHEMISTRY FRONTIERS

CCS 中国化学会
CHINESE CHEMICAL SOCIETY
ICCAS
ROYAL SOCIETY OF CHEMISTRY
rsc.li/frontiers-materials

MATERIALS CHEMISTRY
FRONTIERS

CHINESE CHEMICAL SOCIETY

ROYAL SOCIETY OF CHEMISTRY

REVIEW

View Article Online
View Journal | View Issue

Cite this: *Mater. Chem. Front.*, 2023, 7, 4635

Recent progress in metal halide perovskite photocatalysts for hydrogen evolution

Xing Wang, Yu Peng, Shuang Yang,* Hua Gui Yang and Yu Hou*

Received 28th April 2023,
Accepted 24th August 2023

DOI: 10.1039/d3qm00477e

rsc.li/frontiers-materials

Photocatalytic hydrogen production, which directly converts solar energy into green chemical fuel, has received widespread attention. However, despite significant efforts, the efficiency of conventional photocatalytic materials remains below industrial requirements, owing to the intrinsic limitations such as insufficient light absorption and poor carrier transport capability. Metal halide perovskite (MHP) materials feature superior optoelectronic properties and structural flexibility, rendering them highly attractive candidates for photocatalysis. This review provides a concise introduction to the structural characteristics of MHPs and summarizes their recent progress in the field of photocatalytic hydrogen evolution, including single-component MHPs and MHP-based composites. The review also discuss the current challenges and prospects of MHP photocatalysts, which hold promise for advancing photocatalytic solar-to-hydrogen technology.

1. Introduction

Solar energy is a clean and renewable energy source that is abundant, almost infinite, and widely distributed on earth. However, only 1% of the solar energy received by earth has been effectively used,[1,2] highlighting the importance of finding a suitable solar energy carrier to use this valuable resource more efficiently.[3–5] Hydrogen (H_2) is a clean, non-toxic, colorless, and environmentally friendly fuel without carbon dioxide emissions. Additionally, H_2 offers a broad range of energy applications, including H_2 fuel cells,[6–8] combustible fuels,[9–11] and synthetic chemical materials.[12–14] Thus, H_2 serves as an ideal carrier for solar energy. Among the various solar-to-H_2 conversion methods (*e.g.* photoelectrochemical H_2 evolution, photothermochemical H_2 evolution, and photocatalytic H_2 evolution), photocatalytic H_2 evolution technology, which converts solar energy to H_2 resembling natural photosynthesis, has garnered significant research interests.[15–18]

Photocatalytic H_2 evolution reaction (HER) involves three main steps: (1) absorption of light by a photocatalyst to generate excitons; (2) separation and migration of carriers from the bulk to the surface of the photocatalyst; and (3) reduction and oxidation reactions on the photocatalyst surface. For achieving high-efficiency photocatalytic H_2 evolution, photocatalysts need to meet several requirements. First, appropriate energy levels are thermodynamically necessary for suitable photocatalysts.

Key Laboratory for Ultrafine Materials of Ministry of Education, Shanghai Engineering Research Center of Hierarchical Nanomaterials, School of Materials Science and Engineering, East China University of Science and Technology, Shanghai 200237, China. E-mail: syang@ecust.edu.cn, yhou@ecust.edu.cn

Xing Wang

Xing Wang received his BS degree from East China University of Science and Technology (ECUST) in 2022. He is currently a PhD candidate at the ECUST under the supervision of Prof. Yu Hou. His research focuses on the design and fabrication of stable perovskite for effective photocatalytic hydrogen evolution.

Yu Peng

Yu Peng completed her PhD from Fujian Institute of Research on the Structure of Matter, Chinese Academy of Sciences in 2021. She is currently a postdoctoral research fellow at ECUST. Her research focuses on the rational design of photoactive materials for photocatalysis.

As exemplified by photocatalytic water splitting, the conduction band minimum (CBM) of photocatalysts should locate at a more negative potential than the redox potential of H^+/H_2 (0 V at pH = 0 with respect to the normal hydrogen electrode (NHE)), the valence band maximum (VBM) of photocatalysts should locate at a more positive potential than the oxide potential of O_2/H_2O (1.23 V *versus* NHE), and a minimum bandgap of 1.23 eV is required. In addition, the bandgap of photocatalysts should be narrow enough to make full use of sunlight while satisfying the sufficient overpotential, together with sufficient carrier separation and transport ability. Since the original research of Fujishima and Honda in 1972, a rich variety of semiconductors have been exploited in the field of photocatalytic H_2 evolution, such as TiO_2,[19–21] CdS,[22–24] $SrTiO_3$,[25–27] and g-C_3N_4.[28–30] However, state-of-the-art solar-to-hydrogen (STH) efficiencies of most reported photocatalysts are still around 1%, far below the commercialization requirements, owing to the intrinsic limitations such as insufficient light absorption, poor carrier transport capability, and prevailing electron–hole recombination. In this context, it is highly urgent to develop a new class of photocatalysts with suitable optical and electronic properties for efficient photocatalytic H_2 evolution.

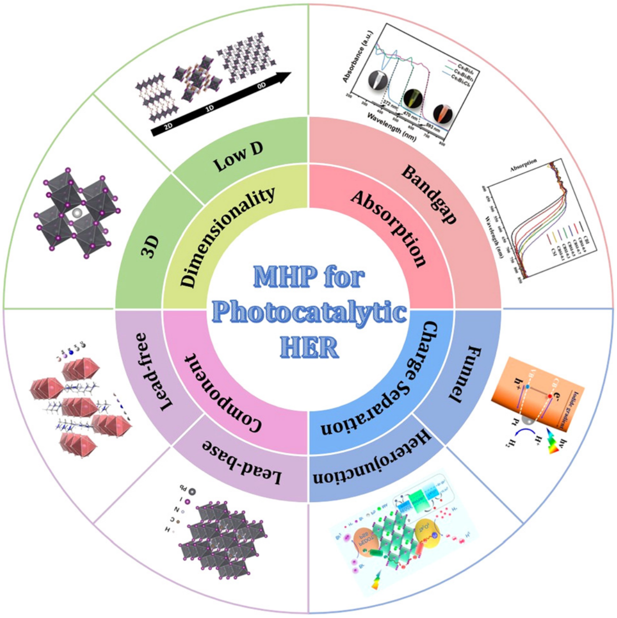

Fig. 1 Schematic overview of metal halide perovskite for photocatalytic hydrogen evolution.

In the past few years, metal halide perovskites (MHPs) have achieved noteworthy breakthroughs in the field of optoelectronics,[31–33] including solar cells,[34–37] light emitting diodes,[38–40] and photodetectors.[41–43] Particularly, the light conversion efficiency (PCE) of MHP-based solar cells reached a record of 25.73%,[44] suggesting the highly efficient light absorption and charge transport abilities of MHP materials. Emphatically, MHP materials have plentiful superiorities for photocatalysts, such as high light absorption coefficient,[45,46] long carrier diffusion lengths, low binding energy,[47,48] tunable bandgaps,[49,50] and low-cost fabrication, rendering MHPs as viable candidates for photocatalytic H_2 evolution.

To date, despite several reviews on MHPs in photocatalysis,[51–53] comprehensive assessments focusing on

Shuang Yang

Shuang Yang obtained his BS degree from Tsingtao University of Science and Technology in 2011 and completed his PhD in 2016 from ECUST. He then conducted postdoctoral research at Nanyang Technological University and University of Nebraska-Lincoln. Currently, he is a professor at ECUST. His research focuses on the chemistry and physics of semiconducting materials and optoelectrical devices.

Hua Gui Yang

Hua Gui Yang obtained his PhD degree from the National University of Singapore in 2005. He joined the University of Queensland in 2007 as a postdoctoral research fellow. After finishing his postdoctoral training, he came back to China and took up a professor position at ECUST at the end of 2008. His research focuses on the rational design and fabrication of functional materials for solar energy conversion.

Yu Hou

Yu Hou completed his BS and PhD from ECUST in 2010 and 2015, respectively. From 2015 to 2017, he worked as a postdoctoral research fellow at ECUST and then joined the Griffith University as a visiting scholar. Currently, he is a professor at ECUST. His research focuses on novel functional materials of thin film-based solar devices and aims at developing new semiconductor absorbers and cell structures towards next-generation photovoltaic technology.

elucidating the crucial relationship between the structure of MHPs (including the intrinsic structure of MHPs and the composites based on MHPs) and their performance in photocatalytic hydrogen evolution have been scarce. In this review, a thorough overview of recent advancements in the field of photocatalytic H_2 evolution is provided, including component engineering, energy band adjustment (*e.g.*, extra halogen element doping), and composite structure (*e.g.*, MHPs/conductor, MHPs/semiconductor). A specific emphasis is placed on elucidating the correlation between the structure of MHP-based photocatalysts and their performance in hydrogen evolution (Fig. 1). Additionally, the review highlights the current challenges and provides valuable perspectives for the further development of halide perovskites in photocatalytic H_2 evolution. This comprehensive review serves as a valuable reference for the design and development of highly efficient and stable MHP-based photocatalysts for H_2 evolution.

2. Structure and properties of metal halide perovskites

MHPs have a general formula ABX_3, where A is a univalent organic or inorganic cation, such as methylamine cation (MA^+), formamidine cation (FA^+), and Cs^+; B site is a divalent metal ion, such as Pb^{2+} and Sn^{2+}; and X is a halogen ion, such as Cl^-, Br^-, and I^-.[54,55] As shown in Fig. 2a, the B site and X site form a $[BX_6]^{4-}$ octahedron, with B at the center and X at the vertices of the octahedron. Then, $[BX_6]^{4-}$ octahedra are connected in three-dimensional (3D) space by sharing vertices to form a 3D network structure. The formability and structural stability of these perovskite-type metal halide materials can be evaluated by tolerance factor *t*, which is calculated as follows:

$$t = \frac{R_A + R_X}{\sqrt{2}(R_B + R_X)}$$

where R_A, R_B, and R_X are the effective ionic radii of ion A, ion B, and ion X in perovskite respectively. In general, to form a stable perovskite structure at room temperature, the *t* values need to be 0.81–1.11. An ideal cubic perovskite will be formed when *t* is 0.9 to 1.0, while the orthorhombic or tetragonal (Fig. 2b and c) may be formed when *t* is larger or smaller.[56]

The introduction of large-sized organic cations at A site can break down the 3D framework, giving rise to low-dimensional perovskites including two-dimensional (2D), one-dimensional (1D), and zero-dimensional (0D) perovskites (Fig. 3).[57] 2D perovskites consist of alternating arrangements of inorganic $[BX_6]^{4-}$ slabs and the interlayer organic molecules. Notably, the formation of 2D perovskites is not affected by the Goldschmidt tolerance factor, allowing for the utilization of an extensive library of organic cations for their preparation. Based on their crystal structure, 2D perovskites can be divided into Ruddlesden–Popper (RP) phase, Dion–Jacobson (DJ) phase, and the alternating cations in the interlayer space (ACI) phase. The structural formula of RP phase 2D perovskite is $A^1{}_2A_{n-1}B_nX_{3n+1}$, where A^1 is a long-chain univalent organic cation such as butylamine cation (BA^+) or phenethylamine cation (PEA^+), and A is a short-chain organic cation such as MA^+ or FA^+. *n* represents the number of inorganic skeleton layers wrapped by long-chain organic cations. When $n = 1$, it represents a single-layer perovskite at the molecular scale, and when $n \geq 2$, it is a multilayer quasi-2D perovskite structure. The structural formula of the DJ phase 2D perovskite is $A^2A_{n-1}B_nX_{3n+1}$, where A^2 represents a long-chain divalent organic cation, such as ethylenediamine cation (EDA^{2+}) or 1,3-propanediamine cation (PDA^{2+}). The structural formula of the ACI phase 2D perovskite is $A^3A_nB_nX_{3n+1}$, where A^3 is limited to some specific univalent organic cations, such as guanidine cation (GA^+) and methylphenethylammonium cation (MPA^+).[58,59]

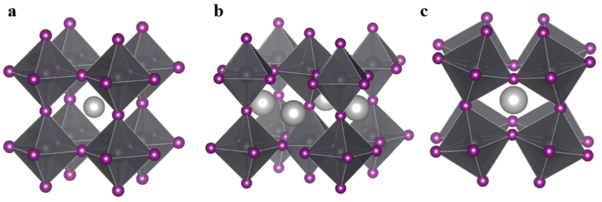

Fig. 2 The different crystal structures of MHPs: (a) cubic structure, (b) tetragonal structure, and (c) orthorhombic structure.

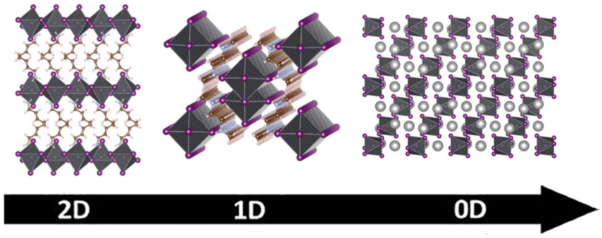

Fig. 3 The crystal structures of 2D, 1D, and 0D perovskite.

Further increase in the size of A-site organic cations will lead to a reduction in the structural dimension of MHPs to 1D and 0D. The structure of 1D perovskites consists of $[BX_6]^{4-}$ octahedra chains with shells of organic cations, such as $[DMEDA]PbBr_4$ (DMEDA = *N*,*N*′-dimethylethylenediamine),[60] and $[TDMP]PbBr_4$ (TDMP = *trans*-2,5-dimethylpiperazine).[61] 0D perovskites are bulk assemblies of individual $[BX_6]^{4-}$ octahedra at the molecular level, where the $[BX_6]^{4-}$ octahedra are separated by organic molecules, such as $(C_9NH_{20})_2SnBr_4$,[62] $(C_4N_2H_{14}Br)_4SnBr_6$.[63]

On the one hand, the electronic dimension of MHPs decreases as the structural dimension decreases from 3D to 0D.[64] Thus, the bandgaps and quantum confinement effect of MHPs increase with decreasing structural dimension, leading to narrower absorption ranges and larger excitation binding energies for low-dimensional MHPs.[31,65] On the other hand, in contrast to 3D MHPs, where the A-site cation is limited to a few cations (including MA^+, FA^+, and Cs^+), low-dimensional MHPs are less limited by the Goldschmidt tolerance factor and compatible with an abundance of functional organic cations such as chiral cations,[66,67] π-conjugated cations,[68,69] and flexible asymmetric cations.[70,71] This facilitates the separation and transportation of photogenerated carriers by reducing the quantum confinement effect and forming a polarization-induced electric field. Furthermore, owing to the hydrophobicity of bulky organic cations, low-dimensional MHPs exhibit much better stability than 3D MHPs, which has been confirmed in a lot of previously reported works.[72–74]

3. Single-component MHP photocatalysts

Driven by their outstanding performance in optoelectronic devices, MHPs have captured significant attention in the field of photocatalysis. However, their susceptibility to moisture poses challenges for their application in photocatalytic water-splitting. Recently, Park *et al.* have found that MHPs can be stabilized in saturated HI solutions, leading to a surge of interest in photocatalytic HI splitting for H_2 production (Fig. 4).[75,76] In comparison to water splitting, which involves four electrons, photocatalytic HI splitting utilizes only two electrons,[77] resulting in an extremely low overpotential.[78,79] Additionally, this reaction presents a feasible alternative to the thermodynamic unfavourable HI thermal decomposition and holds promise for facilitating the industrial iodine-sulphur cycle for H_2 generation.[80] Consequently, there is considerable potential for designing efficient and stable MHPs for photocatalytic HER. In this section, we discuss the progress of single-component MHPs, classified into Pb-based and lead-free MHPs, for photocatalytic H_2 production (Table 1).

3.1 Pb-based perovskites for photocatalytic hydrogen evolution

In 2016, Park *et al.* successfully demonstrated the first photocatalytic HER of MHP by stabilizing $MAPbI_3$ in its saturated HI solution using the dynamic equilibrium between dissolution and precipitation (as shown in Fig. 5a and b). Under visible light excitation, the photogenerated electrons in $MAPbI_3$ reduced H^+ to H_2 and the photogenerated holes oxidized I^- to I_3^-. The oxidized I_3^- ions were subsequently reduced back to I^- by H_3PO_2, achieving sustainable photocatalytic H_2 production. With Pt as co-catalyst, the HER rate and STH efficiency of $MAPbI_3$ (200 mg) were measured to be 11.4 μmol h^{-1} and 0.81%, respectively. This result provided a new solution for the photocatalytic application of MHPs.

Following this approach, halide perovskites with different structures have been explored for photocatalytic HER. For example, Wang *et al.* synthesized three 2D RP perovskites with different lengths of phenylalkylammonium ions ($C_6H_5(CH_2)_nNH_3^+$; n = 1, 2, and 3).[81] In 2D MHP-based solar cells, the 2D MHP layer is consistently oriented parallel to the charge extraction layer, necessitating the passage of carriers through the poorly conductive organic layer for utilization, ultimately resulting in decreased overall charge transport capacity. (Fig. 5d). However, in 2D MHP-based powder photocatalytic systems, carriers traveling along the more conductive inorganic layer can be effectively utilized (Fig. 5e), thus rendering 2D MHPs as promising candidates for photocatalytic HER. Moreover, the excellent moisture resistance of 2D RP MHPs allows the photocatalytic measurement to be carried out in aqueous salt solutions, reducing reliance on strongly acidic HI-saturated solutions. This improvement significantly reduced the acidity of the solution, making the experimental conditions milder, and improved the reproducibility of the measurement due to the lower solubility of 2D perovskite in the aqueous salt solution. Further analysis demonstrated that the length of organic cations could significantly affect the dissolution behaviour, morphology, and photoelectric properties, such as bandgap and band edge position of 2D MHP crystals. Among the investigated 2D MHPs, $(C_6H_5CH_2NH_3)_2PbI_4$ with the shortest length of organic cations showed the best photocatalytic

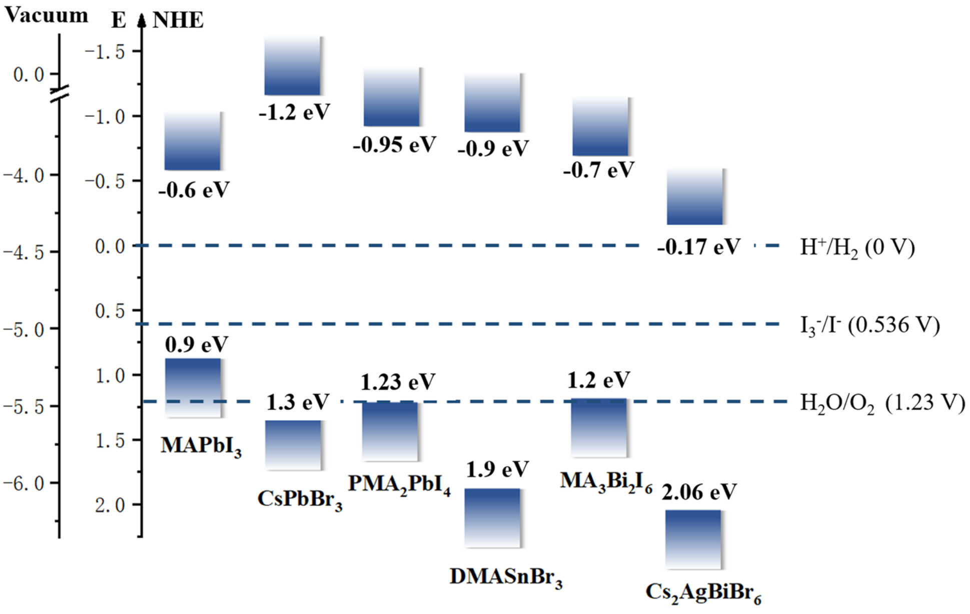

Fig. 4 The schematic diagram of HI splitting with different MHP photocatalysts.[81,83,84]

Table 1 Summary of works on photocatalytic application of MHPs. R = H_2 evolution reaction rate, S = STH efficiency, A = AQE

MHP catalysts	Test conditions	Cocatalysts	MHP usage (mg)	Performance	Year$^{Ref.}$
$MAPbI_3$	Xe lamp ($\lambda \geq 475$ nm) 100 mW cm^{-2} HI solution	Pt	200	R = 11.4 μmol h^{-1} S = 0.81%	2016[75]
$MAPbBr_{3-x}I_x$	Xe lamp (300 W, $\lambda \geq 420$ nm) 100 mW cm^{-2} HI solution	Pt	250	R = 651.2 μmol h^{-1} S = 0.81%	2018[85]
DMA_3BiI_6	LED (λ = 465 nm, 9 mW) HI solution	Pt	500	R = 47 μmol h^{-1} A = 82.8% at 465 nm	2018[86]
$DMASnI_3$	Xe lamp (300 W) DI water	Pt	200	R = 0.64 μmol h^{-1}	2018[87]
$MAPb(I_{0.9}Br_{0.1})_3$	Xe lamp (300 W, $\lambda \geq 420$ nm) 100 mW cm^{-2} The mixed HI/HBr solution	Pt	20	R = 66.69 μmol h^{-1} S = 1.42%	2019[88]
$CsPbBr_{3-x}I_x$	Xe lamp ($\lambda \geq 420$ nm) 120 mW cm^{-2} HI solution	Pt	200	R = 44.8 μmol h^{-1} A = 2.15% at 450 nm	2019[89]
$MAPbI_3$	Xe lamp 120 mW cm^{-2} HI solution Ultrasonication (70 W)	Pt	50	R = 11.2 μmol h^{-1}	2019[90]
2-AMPSbI$_5$ (Sb-precursor is SbI_3)	ABET 103 solar simulator (150 W, λ = 250-1900 nm) 100 mW cm^{-2} Methanol solution (10% vol)		10	R = 1.86 μmol h^{-1}	2019[91]
$MA_3Bi_2I_9$	Xe lamp (300 W, $\lambda \geq 400$ nm) HI solution	Pt	40	R = 6.77 μmol h^{-1} S = 0.48%	2019[92]
$Cs_3Bi_{0.6}Sb_{1.4}I_9$	Simulated sunlight (AM 1.5 G) 100 mW cm^{-2} HI solution	Pt	100	R = 92.6 μmol h^{-1}	2020[93]
$MAPbI_3$ with MA^+ film	Xe lamp (300 W) HI solution		50	R = 15.65 μmol h^{-1}	2021[94]
$(C_6H_5CH_2NH_3)_2PbI_4$	Xe lamp (300 W, $\lambda \geq 420$ nm) HI solution	Pt	150	R = 333 μmol h^{-1} S = 1.57%	2021[81]
$Cs_2Pt_{0.09}Sn_{0.95}Cl_6$	Xe lamp (300 W) TEOA solution (10% vol)	Pt		R = 16.11 μmol h^{-1}	2021[95]
DMA_3BiI_6	LED lamp (100 W) 76.4 mW cm^{-2} HI solution	Pt	50	R = 5.7 μmol h^{-1} A = 0.83% at 535 nm	2021[96]
Defect-rich $Cs_2AgBiBr_6$	Xe lamp (300 W, $\lambda \geq 420$ nm) 332.5 mW cm^{-2} HBr solution		500	R = 0.406 μmol h^{-1}	2021[97]
Cs_2SnI_6	Xe lamp (300 W, $\lambda \geq 420$ nm) 100 mW cm^{-2} HI solution	PtSA	10	R = 4.30 μmol h^{-1}	2021[98]
$FAPbBr_{3-x}I_x$	Xe lamp with an AM1.5G filter (300 W, $\lambda \geq 420$ nm) 100 mW cm^{-2} The mixed HI/HBr solution	PtSA	100	R = 682.6 μmol h^{-1} S = 4.50% A = 33.4% at 530 nm	2022[99]
$OA_{0.15}MA_{0.85}PbI_3$	PL-MW2000 light source in the full visible range HI solution	Pt	5	R = 2.68 μmol h^{-1} A = 1.67% at 420 nm	2022[82]
$MA_3Bi_2Cl_{9-x}I_x$	Xe lamp (300 W, $\lambda \geq 420$ nm) 100 mW cm^{-2} Saturated HCl (or HCl/HI) solution	Pt	500	R = 341 ± 61.7 μmol h^{-1} A = 1.25% at 435 nm	2022[100]
$Cs_3Bi_2I_9$ PNs	Xe lamp (300 W, λ = 350–780 nm, 790 mW cm^{-2}) Ethanol solution		50	R = 10.79 μmol h^{-1}	2022[101]

performance with an HER rate of 333 μmol h^{-1} (150 mg) and an STH efficiency of 1.57% when using Pt as cocatalyst (Fig. 5f).

In addition, Li *et al.* combined the 3D perovskite $MAPbI_3$ with the 2D octadecylammonium lead iodide perovskite (OA_2PbI_4) to create multidimensional perovskites, denoted as $OA_xMA_{1-x}PbI_3$.[82] These materials exhibited superior charge transfer abilities compared to traditional 3D perovskites and better photocatalytic performance than 2D perovskites. Consequently, $OA_xMA_{1-x}PbI_3$ samples showed an optimal photocatalytic HER rate of 2.68 μmol h^{-1} (5 mg), outperforming bare $MAPbI_3$ (1.38 μmol h^{-1}, 5 mg). This excellent performance was ascribed to their superior absorption properties throughout the visible region compared to other $OA_xMA_{1-x}PbI_3$ samples.

Notably, the structural flexibility of MHPs imparts them great potential to tune their energy levels by adjusting halide composition. Huang *et al.* fabricated a mixed halide perovskite $MAPbBr_{3-x}I_x$ (I-doped $MAPbBr_3$) with I gradient distribution in a mixed HI/HBr solution, *via* a light-assisted halide exchange method. In this material, the concentration of I^- increases gradually from the interior to the surface, forming a suitable

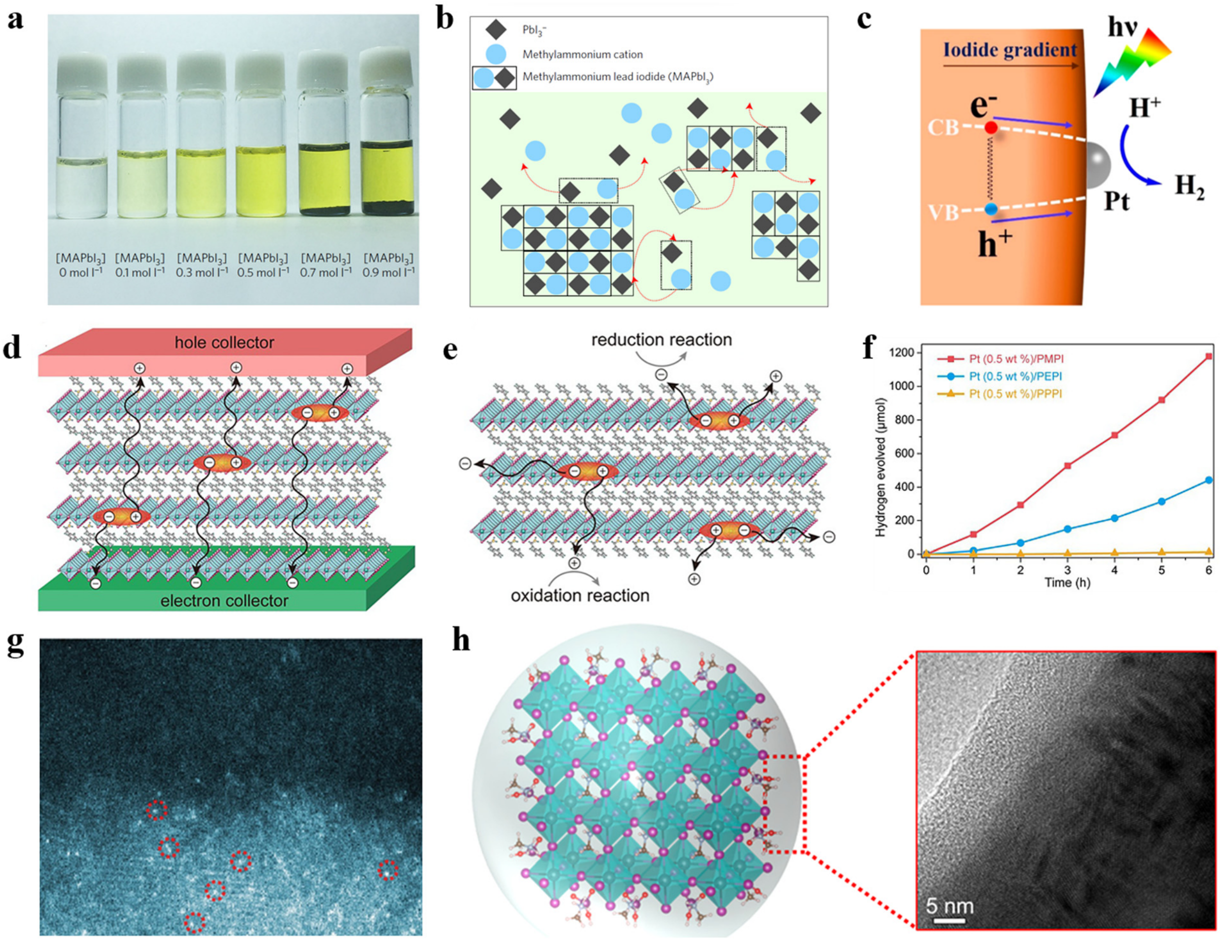

Fig. 5 (a) Photographs of $MAPbI_3$ in different concentrations of HI solution. (b) Diagram of equilibrium dissolution of $MAPbI_3$ powder in saturated HI solution.[75] Copyright 2016 Springer Nature. (c) The funnel bandgap of $MAPbBr_{3-x}I_x$. Copyright 2018 American Chemical Society. The schematic diagram of the migration of carriers for 2D perovskite in (d) solar cell and (e) photocatalyst. (f) The photocatalytic HER rates of $(C_6H_5CH_2NH_3)_2PbI_4$ (PMPI), $(C_6H_5(CH_2)_2NH_3)_2PbI_4$ (PEPI), and $(C_6H_5(CH_2)_3NH_3)_2PbI_4$ (PPPI).[81] Copyright 2021 Wiley-VCH GmbH. (g) The scanning transmission election microscope-high angle annular dark field (STEM-HAADF) images of PtSA/$FAPbBr_{3-x}I_x$. Copyright 2022 Wiley-VCH GmbH. (h) Schematic diagram of the growth of organic passivation membrane on the surface of $MAPbI_3$.[94] Copyright 2021 American Chemical Society.

bandgap funnel structure (Fig. 5c). As a result, $MAPbBr_{3-x}I_x$ exhibited an HER rate of 652.1 μmol h^{-1} (250 mg) and an STH efficiency of 1.05% with the use of Pt as co-catalyst, owing to the bandgap funnel facilitated transfer of photogenerated carriers. Furthermore, Zhao *et al.* tunned the energy levels of $MAPbI_3$ by one-pot crystallization.[88] It should be noticed that there was no bandgap funnel in obtained $MAPb(I_{1-x}Br_x)_3$ (Br-doped $MAPbI_3$) by this method. The synthesized mixed halide perovskite showed a championing HER rate of 66.96 μmol h^{-1} (20 mg) and an outstanding STH efficiency of 1.42% without the use of co-catalysts when $x = 0.1$. This material exhibited great stability without significant decrease in photocatalytic activity over 252 h (63 runs, 4 h per run).

Similarly, Guan *et al.* synthesized an all-inorganic perovskite $CsPbBr_{3-x}I_x$ with a funnel bandgap for photocatalytic HER.[89] The $CsPbBr_{3-x}I_x$/Pt system showed an optimized HER rate of 224 μmol h^{-1}. Moreover, the $CsPbBr_{3-x}I_x$/Pt system also displayed an apparent quantum efficiency (AQE) of 2.15% at 450 nm without obvious decrease in 50 h continuous HER. Such all-inorganic MHPs exhibit better stability compared with organic–inorganic hybrid MHPs, according to the previously reported works in MHPs-based solar cells.[102,103]

Halide perovskites with FA^+ ion as the A cation exhibit significantly longer carrier lifetimes and diffusion lengths compared to those based on MA^+ ion,[104] making them promising candidates for photocatalytic HER. Wu *et al.* investigated the photocatalytic HER performance of Pt single atoms (PtSA) loaded $FAPbBr_{3-x}I_x$ in mixed HBr/HI solution, whose crystal structure and morphology are depicted in Fig. 5g.[99] The PtSAs, which were uniformly distributed on the surface of $FAPbBr_{3-x}I_x$ by coordinating with Br/I ions, decreased the free energy of H* adsorption for Pt/$FAPbBr_{3-x}I_x$ to almost 0 (around 0.04 eV), leading to an enhanced photocatalytic HER rate of 682.6 μmol h^{-1} (100 mg) and an impressive STH efficiency of 4.50%.

In addition, Wang *et al.* demonstrated that ultrasonication could improve the photocatalytic HER performance of $MAPbI_3$, resulting in a 7 times higher photocatalytic HER rate under ultrasonic conditions (23.30 μmol h^{-1}, ultrasonic power = 70 W) than under visible-light conditions alone (3.42 μmol h^{-1}).[90] This enhancement in the HER rate can be attributed to the establishment of a build-in polarized electric field triggered by dipole moments under ultrasonication, which can efficiently separate photogenerated carriers and thus enhance catalytic efficiency.

Though great progress has been made, the water-stability of MHPs remains a critical issue that needs to be addressed. To improve their moisture stability, Liu *et al.* created an organic membrane that effectively passivates $MAPbI_3$, using a light- and solution-based treatment (Fig. 5h).[94] The HIO_3 molecule on the surface of $MAPbI_3$ formed a hydrogen bond with another HIO_3 molecule on the neighbouring $MAPbI_3$ crystal, enhancing the crystallinity of $MAPbI_3$. Moreover, MA^+ was anchored to the surface of the HIO_3 layer by electrostatic interaction with IO_3^-, further enhancing the stability of $MAPbI_3$. In consequence, the photocatalytic HER rate was 2.24-fold enhancement than the bare $MAPbI_3$ without a passivating layer.

3.2 Lead-free perovskites for photocatalytic hydrogen evolution

Despite the impressive achievements of Pb-based perovskites in photocatalytic H_2 production, the toxicity of Pb limits their further application. To address this issue, lead-free perovskites have been explored, involving the replacement of Pb^{2+} with Sn^{2+}, Bi^{3+}, Sb^{3+}, or the substitution of two Pb^{2+} with one univalent metal cation (*e.g.* K^+, Ag^+, and Cu^+) and one trivalent metal cation (*e.g.* Sb^{3+}, Bi^{3+}).[105–107] In this section, the recent advances in lead-free perovskites for photocatalytic HER are discussed.

3.2.1 Sn-based metal halide perovskites. Sn, a non-toxic element possessing a similar electron configuration to Pb, is regarded as a promising substitute for Pb. Ju *et al.* reported the fabrication of a Sn-based halide perovskite, $DMASnI_3$ (DMA = dimethylammonium cation, $CH_3NH_2CH_3^+$) (Fig. 6a), which displayed excellent water stability with no decomposition observed after 16 h of immersion in deionized (DI) water (Fig. 6b).[87] They observed that $DMASnI_3$ crystals exhibited invertible bandgap narrowing behaviour and long carrier lifetimes, indicating enormous potential for optoelectronic applications. However, the HER rate of $DMASnI_3$ crystals was measured to be only 0.64 μmol h^{-1} (Fig. 6c), which could be ascribed to the 1D structure-induced broad bandgap, large effective masses of electrons/holes, and Sn-vacancies induced deep defect states.

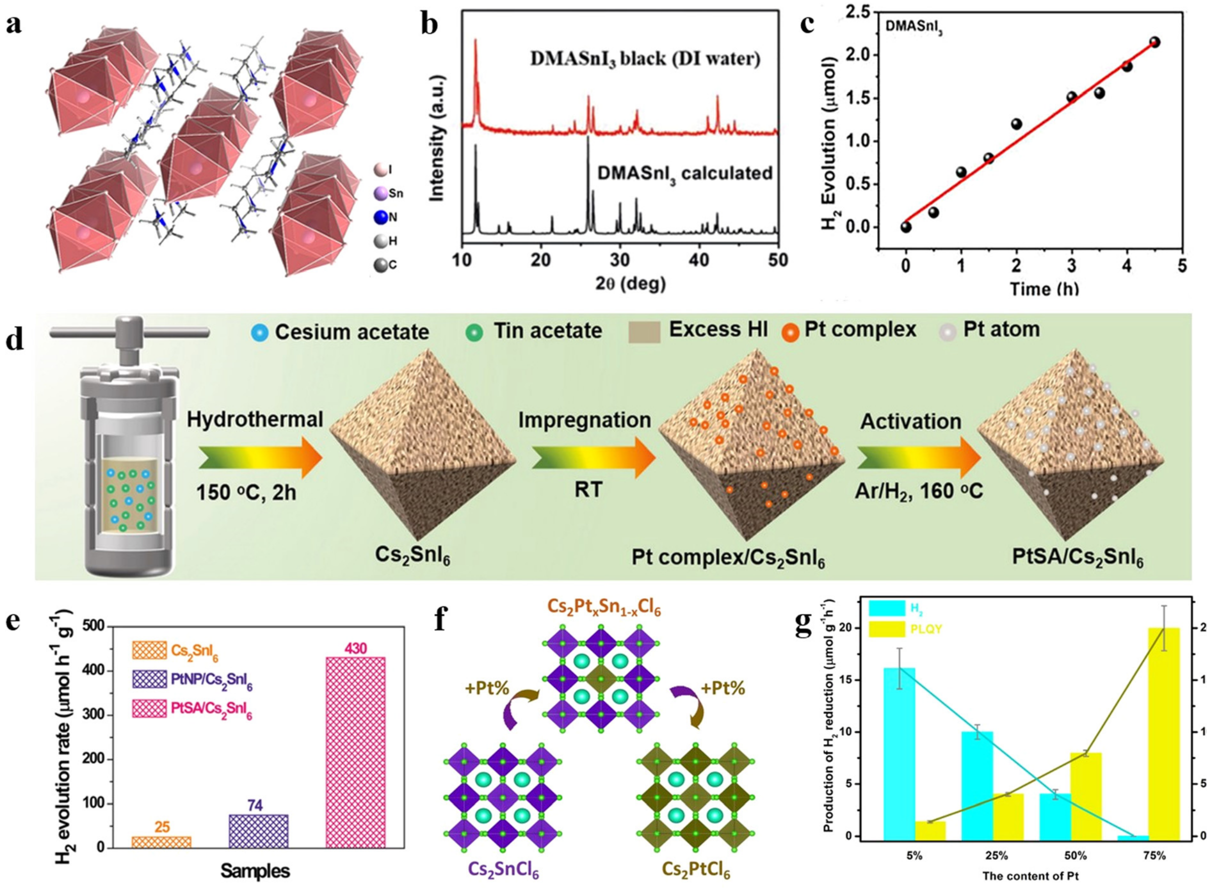

Fig. 6 (a) The crystal structure of $DMASnI_3$. (b) The XRD pattern of black $DMASnI_3$ after treatment of DI water. (c) The photocatalytic HER rate of $DMASnI_3$ in DI water.[87] Copyright 2021 Wiley-VCH GmbH. (d) The schematic diagram of $PtSA/Cs_2SnI_6$ preparation process. (e) The photocatalytic HER rates of Cs_2SnI_6, $PtNP/Cs_2SnI_6$, and $PtSA/Cs_2SnI_6$.[98] Copyright 2021 Springer Nature. (f) The crystal structure of Cs_2SnCl_6 with different Pt doping concentrations. (g) The photocatalytic HER rates and average photoluminescence quantum yields of $Cs_2Pt_xSn_{1-x}Cl_6$ $(0 < x < 1)$.[95] Copyright 2021 Wiley-VCH GmbH.

Furthermore, Zhuo *et al.* synthesized Cs_2SnI_6 perovskite and loaded PtSA on its surface using an impregnation-heat activation method (Fig. 6d).[98] The unique coordination structure and electronic properties of Pt–I_3 sites led to a strong metal–support interaction effect and promoted the photogenerated electron transfer from Cs_2SnI_6 to the PtSA, reducing the Gibbs free energy and accelerating the H_2 generation kinetics. The 0.12 wt% PtSA/Cs_2SnI_6 demonstrated the highest activity for photocatalytic H_2 production, with a rate of 4.30 μmol h^{-1} (10 mg), which was 17.2- and 5.8-fold enhancement than that of pure Cs_2SnI_6 and optimized 3.88 wt% Pt nanoparticle/Cs_2SnI_6, respectively (Fig. 6e).

Yin *et al.* employed a hydrothermal method to partially replace Sn^{4+} in Cs_2SnI_6 with Pt^{4+} to obtain a range of highly stable $Cs_2Pt_xSn_{1-x}Cl_6$ perovskites, where Cs^+, Cl^-, Sn^{4+}, and Pt^{4+} ions were uniformly distributed (Fig. 6f).[95] Among them, $Cs_2Pt_{0.05}Sn_{0.95}Cl_6$ demonstrated remarkable phase stability in water for 25 days and exhibited an excellent photocatalytic HER rate (16.11 μmol h^{-1}). Interestingly, the photocatalytic function of $Cs_2Pt_xSn_{1-x}Cl_6$ could be fine-tuned by controlling the amount of Pt^{4+} (Fig. 6g). As the amount of Pt^{4+} increased, the photocatalytic HER performance of $Cs_2Pt_xSn_{1-x}Cl_6$ decreased.

3.2.2 Bi- and Sb-based metal halide perovskites.

Bi^{3+} with lone-pair $6s^2$ exhibits a similar outer electronic configuration as Pb^{2+}. Owing to their shallow carrier traps and excellent transport properties, Bi-based MHPs have emerged as promising candidates for lead-free halide perovskite photocatalysts. In this context, Zhao *et al.* synthesized a crystalline photocatalyst DMA_3BiI_6 *via* a solvothermal method (Fig. 7a).[86] Photocatalytic measurements were carried out in its well-dispersed HI-H_3PO_2 system containing separated Pt ions and $[BiI_6]^{3-}$ ions. When irradiated at 465 nm, the Pt/DMA_3BiI_6 photocatalytic system exhibited a superior AQE of ~82.8% for photocatalytic H_2 production, achieving an impressive photocatalytic HER rate of 47 μmol h^{-1} (500 mg) and showing stable activity without obvious decrease over 100 h. This high activity could be attributed to the efficient separation of carriers at the interface between $[BiI_6]^{3-}$ and Pt ions.[108] In a subsequent study, they

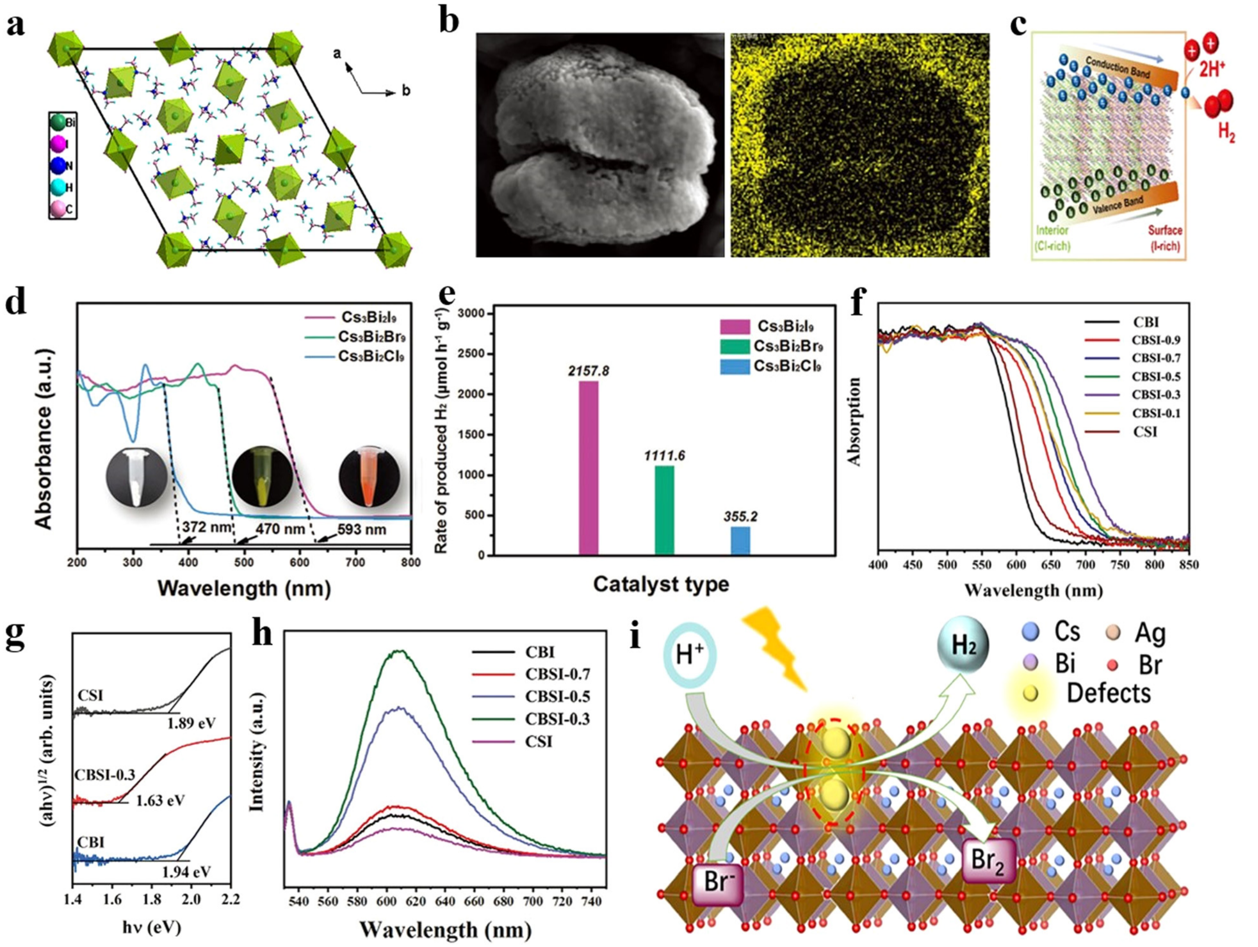

Fig. 7 (a) The crystal structure of DMA_3BiI_6.[86] Copyright 2018 Elsevier. (b)The SEM image (left) and EDS mapping (right) for I of $MA_3Bi_2Cl_{9-x}I_x$. (c) The funnel bandgap of $MA_3Bi_2Cl_{9-x}I_x$.[100] Copyright 2022 Wiley-VCH GmbH. (d) ultraviolet-visible diffuse reflection spectra (UV-vis DRS) of $Cs_3Bi_2X_9$ (X = Cl, Br, I) (the inset are physical photographs of them). (e) The photocatalytic HER rates of $Cs_3Bi_2X_9$ (X = Cl, Br, I).[101] Copyright 2022 Wiley-VCH GmbH. (f) The UV-vis DRS of $Cs_3Bi_{2x}Sb_{2-2x}I_9$ with different *x*. (g) Optical absorptions of $Cs_3Bi_2I_9$, $Cs_3Sb_2I_9$, and $Cs_3Bi_{0.6}Sb_{1.4}I_9$. (h) The steady-state photoluminescence spectra of $C_{s3}Bi_2I_9$, $Cs_3Sb_2I_9$, and $Cs_3Bi_{0.6}Sb_{1.4}I_9$.[93] Copyright 2020 Wiley-VCH GmbH. (i) The schematic diagram of photocatalytic HER on defect-rich $Cs_2AgBiBr_6$.[97] Copyright 2021 American Chemical Society.

found that DMA_3BiI_6 could be stabilized in the aqueous DMAI solution for at least two weeks without additional acids or coatings, through a dissolution–recrystallization process of DMA_3BiI_6 surface molecules.[96] However, the photocatalytic performance of DMA_3BiI_6 in the DMAI solution was unsatisfactory, showing an HER rate of 4.55 μmol h^{-1} (50 mg) and an AQE of 0.83% at 535 nm with Pt as the co-catalyst.

Furthermore, Guo *et al.* synthesized a Bi-based perovskite $MA_3Bi_2I_9$ using a facile hydrothermal method, which displayed a photocatalytic HER rate of 6.77 μmol h^{-1} (40 mg) and an STH efficiency of 0.48%.[92] Additionally, it displayed no obvious decrease in HER rate after a 70 h test. In the later study, Tang *et al.* developed a mixed halide perovskite $MA_3Bi_2Cl_{9-x}I_x$ in which the iodine element exhibited a gradient distribution (Fig. 7b). The $MA_3Bi_2Cl_{9-x}I_x$ possessed a funnel bandgap (Fig. 7c), which could efficiently promote the migration of photogenerated carriers from the bulk to the surface to participate in the photocatalytic redox reaction.[100] Consequently, the HER rate of $MA_3Bi_2Cl_{9-x}I_x$ (500 mg) was significantly improved to 341 ± 61.7 μmol h^{-1} with Pt as the co-catalyst.

Ji *et al.* fabricated a number of $Cs_3Bi_2X_9$ perovskites, where X represents Cl, Br, or I.[101] They observed that the absorption range of $Cs_3Bi_2X_9$ increases with the atomic number of halogens (Fig. 7d). Additionally, the Bi–Bi distance in the octahedral units gradually decreases from $Cs_3Bi_2Cl_9$ to $Cs_3Bi_2I_9$, alleviating the strong confinement effect of electron–hole pairs and accelerating the separation and transfer of photogenerated charges. Consequently, $Cs_3Bi_2I_9$ with the higher light absorption exhibited the most outstanding photocatalytic activity, with an HER rate of 107.89 μmol h^{-1} (50 mg) in ethanol solution (Fig. 7e).

In contrast, under I-rich and Bi-poor conditions, Bi^{3+} vacancies readily appear in Bi-based perovskites with the formation energy of 1.34 eV.[93] These vacancies form deep energy levels within the band gap, impeding the separation of photogenerated carriers and serving as sites for recombination. To confront this challenge, Chen *et al.* introduced Sb into $Cs_3Bi_2I_9$ and obtained $Cs_3Bi_{2x}Sb_{2-2x}I_9$.[93] The theoretical calculation confirmed that the addition of Sb resulted in a lower participation of Bi^{3+} in the conduction band, which weakened the impact of Bi vacancies on the band structure. This effect was reflected in the narrower band gap and fewer intermediate band of $Cs_3Bi_{2x}Sb_{2-2x}I_9$ than pure $Cs_3Bi_2I_9$ and $Cs_3Sb_2I_9$ (Fig. 7f–h), which significantly improved its performance of H_2 evolution reaction, with an optimal HER rate of 92.6 μmol h^{-1} (100 mg) among all reported lead-free perovskites.

Additionally, He *et al.* prepared a defect-rich $Cs_2AgBiBr_6$ by inducing surface defects by visible light, which exhibited better photocatalytic efficiency than $Cs_2AgBiBr_6$.[97] The defect-rich $Cs_2AgBiBr_6$ exhibited an HER rate of 0.406 μmol h^{-1} (500 mg), surpassing that of pure $Cs_2AgBiBr_6$ (0.04 μmol h^{-1}, 500 mg), and exhibited no performance degradation after an 80 h photocatalytic HER.

Similarly, the Sb element, which is adjacent to Pb, also contains ns^2 lone pair electrons and exhibits stable positive trivalent state, making it a promising alternative to Pb.[109] Rokesh *et al.* synthesized a new organic–inorganic hybrid perovskite, named 2-(aminomethyl pyridine)SbI_5 (2-$AMPSbI_5$), *via* sol–gel method.[91] The 2-$AMPSbI_5$, using Sb-iodide precursors, displayed a promising HER rate (1.86 μmol h^{-1}, 10 mg) in ethanol solution.

4. MHP-based composite photocatalysts

4.1 Band structure of composite photocatalysts

To enhance the separation of photogenerated carriers, composite photocatalysts with heterogeneous structures have been investigated. These composite photocatalysts often consist of a combination of photocatalysts with other materials, including conductors, semiconductors, and insulators. Among the various composites, heterojunctions formed between semiconductors have received significant attention, primarily categorized into I-type, II-type, Z-type, and S-type heterojunctions.

The band arrangement of two semiconductors in a I-type heterojunction is straddling. When exposed to light, photogenerated carriers are transferred from the wide-bandgap semiconductor to the semiconductor with lower conduction and higher valence bands to participate in the photocatalytic reaction (Fig. 8a).[110] In contrast, the band arrangement of two semiconductors in a II-type heterojunction is staggered. Under illumination, electrons transfer to the lower conduction band, while holes transfer to the higher valence band, both actively participating in the photocatalytic reaction (Fig. 8b).[111] Although the II-type heterojunction enhances charge carrier separation, it comes at the expense of the oxidation–reduction capacity of the two semiconductors. Z-type heterojunctions, named for their photogenerated carrier transfer process resembling the letter ''Z'', share a similar structure with II-type heterojunctions.[112] However, oxidation and reduction reactions occur in semiconductors with higher conduction band and lower valence band, respectively. The remaining electrons and holes are recombined indirectly or interactively (Fig. 8c). The S-type heterojunction originates from the band bending that

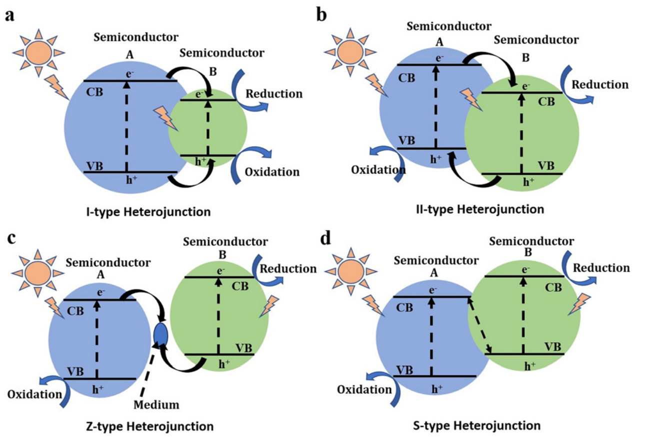

Fig. 8 Schematic diagrams of semiconductor heterojunctions. (a) I-type heterojunction. (b) II-type heterojunction. (c) Z-type heterojunction. (d) S-type heterojunction.

Table 2 Summary of works on photocatalytic application of MHP-based composite catalysts. *R* = H_2 evolution reaction rate, *S* = STH efficiency, *A* = AQE

Composite catalysts	Test conditions	Total catalyst usage (mg)	Performance	Year[Ref.]
Pt(0.75 wt%)@TiO_2/$MAPbI_3$	Xe lamp (300 W, $\lambda \geq 420$ nm) 200 mW cm^{-2} HI solution	15	R = 79.4 μmol h^{-1} S = 0.86% A = 70% at 420 nm	2018[113]
$CsPbBr_3$/Ru@TiO_2	Continuous wave (CW) laser (445 nm, 50 mW) Trifluoroacetic acid/triethylamine	3.2	R = 30.72 μmol h^{-1} A = 0.4 ± 0.1% at 445 nm	2018[114]
5% rGO/$MAPbI_3$	Xe lamp (300 W, $\lambda \geq 420$ nm) 120 mW cm^{-2} HI solution	100	R = 93.9 μmol h^{-1} A = 1.5% at 450 nm	2018[115]
1.2% BP/$MAPbI_3$	Xe lamp (300 mW cm^{-2}, $\lambda \geq 420$ nm) 25.3 mW cm^{-2} HI solution	30	R = 112.26 μmol h^{-1} S = 0.93% A = 1.5% at 450 nm	2019[116]
15% Ni_3C/$MAPbI_3$	Xe lamp (300 mW cm^{-2}, $\lambda \geq 420$ nm) 100 mW cm^{-2} HI solution	50	R = 118.1 μmol h^{-1} S = 0.91% A = 16.6% at 420 nm	2019[117]
$MAPbBr_3$@Pt/Ta_2O_5/PEDOT:PSS	Xe lamp (300 W, $\lambda \geq 420$ nm) 150 mW cm^{-2} HBr solution	157.5	R = 105 μmol h^{-1} A = 16.4% at 420 nm	2019[118]
2.5% rGO/$Cs_2AgBiBr_6$	Xe lamp (300 W, $\lambda \geq 420$ nm) HBr solution	200	R = 9.78 μmol h^{-1} A = 0.16% at 450 nm	2020[119]
g-C_3N_4/$Cs_3Bi_2I_9$ (10 : 0.1 wt%)	Xe lamp (450 W) equipped with a water-filter and a WG320-filter Methanol solution (10% vol)	6	R = 5.52 μmol h^{-1}	2020[120]
Pt(1.25 wt%)@TiO_2/$EtbtBi_2I_{10}$/rGO	Xe lamp (300 W) HF solution	61	R = 16.76 μmol h^{-1}	2020[121]
CPD(1 wt%)/$MAPbI_3$/Pt(2 wt%)	Xe lamp (300 W, $\lambda \geq 420$ nm, 300 mW cm^{-2}) 100 mW cm^{-2} HI solution	103	R = 1184.2 μmol h^{-1} S = 2.15% A = 53.6% at 420 nm	2020[122]
MoS_2 NSs/$MAPbI_3$	White-light LED lamps (10 W × 9, 380 nm $\leq \lambda \leq$ 780 nm, 450 mW cm^{-2}) HI solution	105	R = 206.1 μmol h^{-1}	2020[123]
$MA_3Bi_2I_9$/DMA_3BiI_6	Xe lamp (300 W, $\lambda \geq 420$ nm) HI solution	200	R = 39.64 μmol h^{-1}	2020[124]
$MAPbI_3$/CoP	Xe lamp (150 W, $\lambda \geq 420$ nm) HF solution	*ca.* 3.12	R = 6.5 μmol h^{-1}	2020[125]
$MAPbI_3$-MC/ML-MoS_2	Xe lamp (300 W, $\lambda \geq 420$ nm) 100 mW cm^{-2} HI solution	100	R = 1360 μmol h^{-1} S = 1.09%	2020[126]
MoS_2(20 wt%)/$MA_{0.6}FA_{0.4}PbI_3$	Xe lamp ($\lambda \geq 420$ nm, 300 mW cm^{-2}) 35 mW cm^{-2} HI solution	50	R = 66.4 μmol h^{-1} S = 0.87% A = 14.5% at 550 nm	2020[127]
$DMASnBr_3$(33 wt%)/g-C_3N_4@Pt(3 wt%)	Xe lamp (1500 W, 300–800 nm, 500 W m^{-2}) equipped with UV outdoor filter TEOA solution (10% vol)	21	R = 36.33 μmol h^{-1}	2021[128]
NiCoB/$MAPbI_3$	Xe lamp (300 W, $\lambda \geq 420$ nm) HI solution	65	R = 170.7 μmol h^{-1} A = 1.96% at 450 nm	2021[129]
$Cs_3Bi_2Br_9$/g-C_3N_4	Xe lamp (1500 W, 300-800 nm, 500 W m^{-2}) equipped with UV outdoor filter TEOA solution (10% vol)	21	R = 22.05 μmol h^{-1}	2021[130]
$MAPbI_3$/MoS_2 nanoflowers	Xe lamp (280 W, $\lambda \geq 420$ nm, 410 mW cm^{-2}) 100 mW cm^{-2} HI solution	50	R = 1469.45 μmol h^{-1} S = 7.35% A = 22.1% at 500 nm	2021[131]
$Cs_2AgBiBr_6$/N-C	Xe lamp (300 W, $\lambda \geq 420$ nm) 100 mW cm^{-2} HBr solution	10	R = 3.8 μmol h^{-1} A = 0.59% at 420 nm	2021[132]
$MAPbI_3$/PANI NWs	White-light LED lamps (10 W, 380 nm $\leq \lambda \leq$ 780 nm) HI solution	107	R = 38.8 μmol h^{-1} A = 0.3% at 420 nm	2021[133]
$Cs_2AgBiBr_6$/MoS_2(20 wt%)	Xe lamp (300 W, $\lambda \geq 420$ nm, 300 mW cm^{-2}) 41 mW cm^{-2} HBr solution	50	R = 4.375 μmol h^{-1} A = 0.2% at 450 nm	2022[134]
$CsPbBr_3$(30 wt%)/ZIF-8	Xe lamp (300 W) Na_2SO_3 DI water solution	300	R = 2.36 μmol h^{-1}	2022[135]
g-C_3N_4/$Cs_2AgBiBr_6$ (1 : 10 wt%)	Xe lamp (300 W, $\lambda \geq 420$ nm) HBr solution	50	R = 3 μmol h^{-1}	2022[136]
NiCoP(12.5% wt%)/$Cs_2AgBiBr_6$	Xe lamp (300 W, $\lambda \geq 420$ nm) HBr solution	100	R = 37.32 μmol h^{-1}	2022[137]
$CsPbBr_3$/GO-Pt	Xe lamp (300 W, $\lambda \geq 400$ nm) Aromatic alcohol	10	R = 10.6 μmol h^{-1}	2022[138]

occurs at the interface of two semiconductors, which resembles the shape of the letter "S", and its internal charge transfer is akin to the Z-type heterojunction (Fig. 8d).[139] Both S-type and Z-type heterostructures effectively promote charge transfer without compromising the respective oxidation and reduction capabilities of the two semiconductors, garnering considerable research interest in recent years.[140–143] Meanwhile, the redox reaction is separated in space, and it is therefore expected to achieve an efficient overall water splitting through the appropriate medium and test system.[77]

In order to improve the hydrogen production performance of MHP-based photocatalysts, various composite structures have been constructed, such as black phosphorus/$MAPbI_3$ I heterojunction,[116] $MAPbI_3/MoS_2$ II heterojunction,[131] *etc.* (Table 2). In the following section, we mainly introduce the applications of MHP/conductor or MHP/semiconductor composites in the photocatalytic HER.

4.2 Metal halide perovskite/0D nanoparticles composites

4.2.1 Metal oxide nanoparticles. TiO_2 is often used as an electron transport layer in perovskite solar cells due to its good energy level alignment with MHP materials,[144,145] making MHPs/TiO_2 composite systems highly promising for photocatalytic HER. Pavliuk *et al.* first prepared a $Pt@TiO_2/CsPbBr_3$ composite photocatalyst in which $CsPbBr_3$ and $Pt@TiO_2$ acted as solar-light harvesters and photocatalysts (Fig. 9a), respectively. Triethylamine and trifluoroacetic acid were employed as a sacrificial agent and an electron donor, respectively, to stabilize $CsPbBr_3$. As a result, the $Pt@TiO_2/CsPbBr_3$ system demonstrated an HER rate of approximately 30.72 μmol h^{-1} (3.2 mg) and an STH efficiency of about 0.4%. Similarly, Wang *et al.* established a TiO_2 electron-transporting channel between Pt and $MAPbI_3$.[113] This combination resulted in a significant elevation in the photocatalytic HER rate of 79.4 μmol h^{-1} (15 mg), an approximately 89-fold increase compared to the HER rate of Pt/$MAPbI_3$. Additionally, the AQE of HER was about 70% at 420 nm, and the STH efficiency was approximately 0.86%. Furthermore, Ta_2O_5 nanoparticles were loaded with Pt and then combined with $MAPbI_3$ as $Ta_2O_5/MAPbI_3$/Pt composite photocatalyst, which exhibited an HER rate of 39.9 μmol h^{-1} (15 mg).[113]

In a subsequent study, Wang *et al.* prepared a $MAPbBr_3@Pt/Ta_2O_5$/PEDOT:PSS composite photocatalyst by simultaneously introducing a photogenerated electron extractor (Ta_2O_5) and a photogenerated hole extractor (PEDOT:PSS) (Fig. 9b).[118] By combining $MAPbBr_3$ with Pt/Ta_2O_5 and PEDOT:PSS, electron and hole transport channels were established, which greatly improved the charge transport efficiency and realized efficient catalytic reactions. Consequently, the HER rate of the $MAPbBr_3@Pt/Ta_2O_5$/PEDOT:PSS composite photocatalyst (105 μmol h^{-1}, 157.5 mg) was 52-fold higher than that of pristine $MAPbBr_3$, emphasizing the outstanding advantages of establishing a dual charge transport highway for improving the photocatalytic performance of MHP materials.

4.2.2 Transition metal carbide nanoparticles. Ni_3C, as an earth-abundant and fascinating iron group transition metal carbide, has demonstrated exceptional photocatalytic activity for H_2 production in acidic conditions.[146–148] Through a simple surface charge-promoted self-assembly technique, Zhao *et al.* synthesized a $MAPbI_3/Ni_3C$ composite photocatalyst.[117] Scanning electron microscope (SEM) images showed that Ni_3C was loaded on the surface of $MAPbI_3$ (Fig. 9c). The photocatalytic process of this composite is shown in the Fig. 9d. The HER rate of 15% $Ni_3C/MAPbI_3$ reached 118.1 μmol h^{-1} (50 mg),

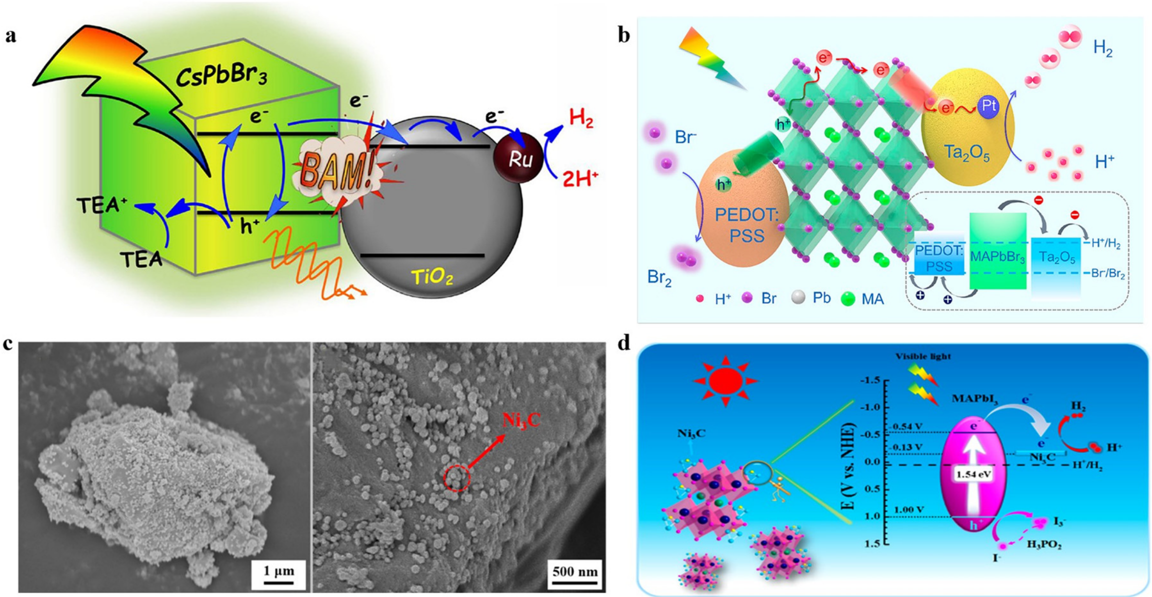

Fig. 9 (a) The schematic diagram of photocatalytic HER on $Pt@TiO_2/CsPbBr_3$ in TEOA solution.[114] Copyright 2018 Elsevier. (b) The schematic diagram of photocatalytic HER on $Pt@Ta_2O_5/MAPbBr_3$/PEDOT:PSS in HBr solution.[118] Copyright 2019 American Chemical Society. (c) SEM images of $Ni_3C/MAPbI_3$. (d) The mechanism of photocatalytic HER of $Ni_3C/MAPbI_3$.[117] Copyright 2019 American Chemical Society.

which was about 55-fold enhancement than that of $MAPbI_3$ (2.15 μmol h^{-1}, 50 mg) and far higher than that of Pt/$MAPbI_3$ (26.7 μmol h^{-1}, 50 mg). Notably, the photocatalytic HER rate of $Ni_3C/MAPbI_3$ showed no obvious decrease after a designed photoreaction process involving 10 cycles, one-month storage, and an additional 10 cycles, highlighting the superb stability of this composite photocatalyst. The excellent photocatalytic HER activity and stability of $Ni_3C/MAPbI_3$ were believed to originate from the improved carrier separation and transfer ability, the increased number of reaction sites on the surface of $MAPbI_3$, and the intrinsic stability of the composite photocatalyst.

4.2.3 Transition metal phosphide nanoparticles. Transition metal phosphides are hopeful substitutes for noble metal cocatalysts to enhance the outstanding carriers' separation and migration capacity and enable low-cost production.[149–151] Using a simple *in situ* photosynthesis method, Cai *et al.* first synthesized a $MAPbI_3$/cobalt phosphide (CoP) composite structure.[125] CoP nanoparticles could be used as cocatalysts as they can not only effectively extract photoinduced electrons from $MAPbI_3$ and enhance the separation of carriers but also promote interfacial photocatalytic reactions. Based on these advantages, the $MAPbI_3$/CoP composite photocatalyst exhibited an excellent HER rate of *ca.* 2.45 μmol h^{-1} (*ca.* 3.12 mg) in HI solution within 3 h, which was about 8-fold enhancement than that of bare $MAPbI_3$. Moreover, when the photocatalytic reaction time increased to 27 h, its HER rate reached *ca.* 6.5 μmol h^{-1} (*ca.* 3.12 mg), which could be attributed to the ameliorative crystallinity of $MAPbI_3$ and the increased reaction active sites of CoP co-catalyst during the incessant photocatalytic reaction. Furthermore, Huang *et al.* developed a NiCoP/$Cs_2AgBiBr_6$ composite photocatalyst *via* the electrostatic coupling method.[137] With visible-light irradiation, NiCoP acted as an electron extractor to improve the charge separation efficiency of $Cs_2AgBiBr_6$, thereby boosting the photocatalytic H_2 production ability. Specifically, the composite photocatalyst displayed a maximum HER rate of 37.32 μmol h^{-1} (100 mg) at a loading amount of 12.5% NiCoP, with approximately 88-fold enhancement over that of pristine $Cs_2AgBiBr_6$. In addition, transition metal phosphides are economical and environmentally friendly, favouring their further development.

4.2.4 Carbon-based nanomaterials. Being part of the carbon-based nanomaterial family, carbonized polymer dots (CPDs) exhibit exceptional potential in enhancing the photocatalytic HER activity of MHP owing to their high photochemical stability, outstanding photophysical, and chemical properties.[152,153] Zhao *et al.* developed a hybrid photocatalytic system by combining Pt/$MAPbI_3$ with CPDs synthesized from citric acid (CA) and *p*-aminosalicylic acid (PASA), in which the CPDs acted as efficient photogenerated hole extractors. Benefiting from the well-matched energy levels, the optimized Pt/$MAPbI_3$/CA-PASA CPD hybrid photocatalytic system exhibited an outstanding HER rate of 1184.2 μmol h^{-1} (103 mg), an STH efficiency of 2.15%, and an AQE of 53.6% at 420 nm.

4.3 Metal halide perovskite/2D vdW material composites

In recent years, 2D van der Waals (vdW) materials have demonstrated promising potential in the field of photocatalysis. The advantages of using 2D vdW materials can be summarized as follows: (1) the 2D nature of these materials leads to unique electronic properties that can enhance electron transport and improve charge transfer capacity; (2) the atomic-scale thickness can effectively shorten the carrier diffusion distance and improve carrier utilization; (3) the inherently large specific surface area is beneficial for the adsorption and activation of reactive molecules. Thus, combining MHPs with 2D vdW materials provides great potential for photocatalytic HER.

4.3.1 Graphene derivatives. Graphene derivatives, such as graphene oxide (GO) and reduced graphene oxide (rGO), which hold good electron transfer properties and acid stability,[154–156] have been utilized in MHP-based composites to improve the HER performance of MHP. For instance, Wu *et al.* synthesized a $MAPbI_3$/rGO composite using a photoreduction method.[115] SEM images showed that rGO was loaded on the surface of $MAPbI_3$. During photocatalytic HER, photoinduced electrons in $MAPbI_3$ were transferred to rGO *via* the Pb–O–C bond to participate in the reduction of H^+ at the rGO position, and photogenerated holes oxidized I^- to I_3^- (Fig. 10a). Consequently, the $MAPbI_3$/rGO composite displayed an enhanced HER rate of 93.9 μmol h^{-1} (100 mg), which was 67-fold enhancement than that of bare $MAPbI_3$. In another study, Chen *et al.* first demonstrated the selective oxidation of aromatic alcohol to the aromatic aldehyde using $CsPbBr_3$/GO-Pt composite, accompanied by HER.[138] GO with abundant functional groups induced the nucleation process of $CsPbBr_3$, leading to the smaller size perovskite nanocrystals. Additionally, GO-Pt acted as photogenerated electron extractors, inhibiting the recombination of electron–hole pairs. Consequently, the optimized $CsPbBr_3$/GO-Pt exhibited an HER rate of 10.6 μmol h^{-1} (10 mg) with high selectivity (>99%) for benzyl aldehyde generation (10.5 μmol h^{-1}, 10 mg) under visible light, which was about 5-fold enhancement than that of the $CsPbBr_3$-Pt sample.

Liu *et al.* reported a 0D lead-free perovskite $(Etbt)_4Bi_2I_{10}$ (Etbt = 3-ethylbenzo[*d*]thiazol-3-ium) and constructed a $(Etbt)_4Bi_2I_{10}$-based composite photocatalyst by introducing Pt/TiO_2 and rGO as an electron extractor and a hole extractor, respectively.[121] Unlike conventional protonated cations, Etbt does not contain conventional hydrogen-bond donors, which helps prevent hydrogen-bonding interactions from eroding hybrid perovskites. Consequently, $(Etbt)_4Bi_2I_{10}$ showed outstanding stability in DI water, acid solution, and ultraviolet light, achiving a potential HER rate of 0.736 μmol h^{-1} (130 mg) with 0.5 wt% Pt nanoparticles loading. After incorporating Pt/TiO_2 and rGO to achieve a dual-charge transport-modulated composite photocatalyst, the photocatalytic system showed a significantly improved HER rate of 16.76 μmol h^{-1} (61 mg). In a later study, Wang *et al.* combined $Cs_2AgBiBr_6$ with rGO by a photo-reduction process and applied it for HER in a saturated HBr aqueous solution.[119] The $Cs_2AgBiBr_6$/rGO with optimal rGO loading displayed improved photocatalytic performance compared to that of pure $Cs_2AgBiBr_6$, which could be attributed to the promoted separation and migration of carriers by rGO. The HER rate reached 9.78 μmol h^{-1} (200 mg) under

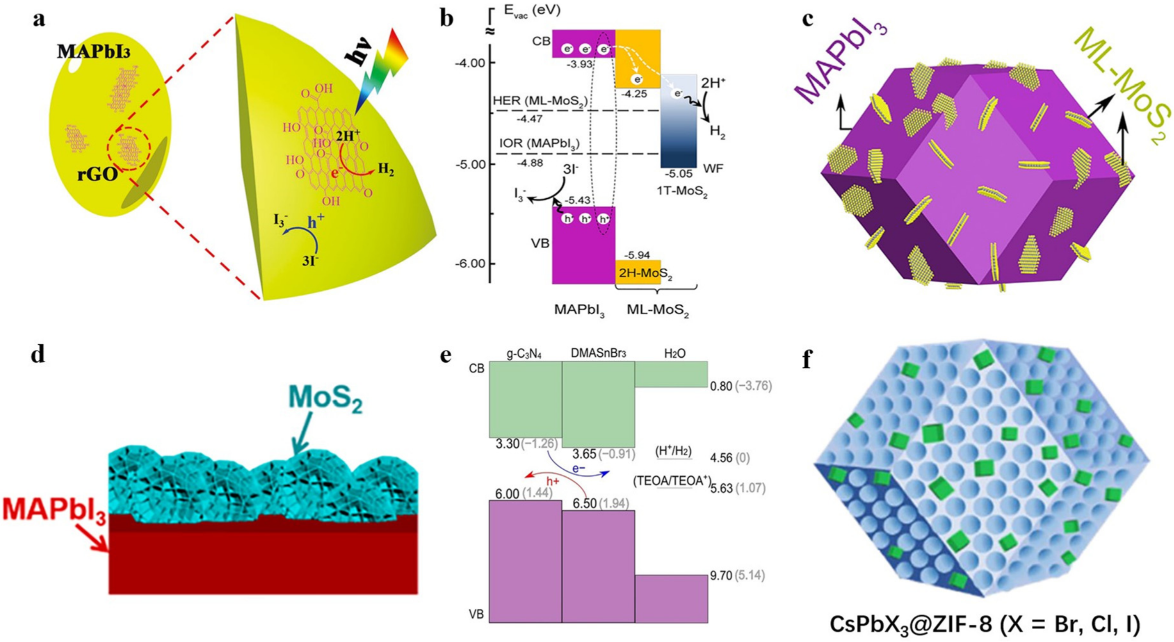

Fig. 10 (a) The schematic diagram of photocatalytic HER on MAPbI3/rGO.[115] Copyright 2018 Wiley-VCH GmbH. (b) The schematic diagram of photocatalytic HER on ML-MoS_2/$MAPbI_3$-MCs. (c) The schematic illustration of structure of ML-MoS_2/$MAPbI_3$-MCs.[126] Copyright 2020 Elsevier. (d) The schematic illustration of structure of MoS_2 nanoflowers/$MAPbI_3$ microcrystals.[131] Copyright 2021 American Chemical Society. (e) The schematic mechanism of photocatalytic HER on g-C_3N_4@$DMASnBr_3$/Pt in triethanolamine solution.[128] Copyright 2018 Wiley-VCH GmbH. (f) The schematic illustration of structure of $CsPbX_3$@ZIF-8 (X = Br, Cl, I).[135] Copyright 2022 American Chemical Society.

visible light irradiation, without significant decrease for 120 h continuous photocatalytic HER.

4.3.2 Molybdenum disulphide. MoS_2 is a layered material that contains unsaturated sulphur, providing plentiful active sites for H_2 at the edges.[157–160] Owing to its specific structure and properties, MoS_2 has been combined with various semiconductors to improve their catalytic performance in HER.[161,162] Wang *et al.* demonstrated the *in situ* coupling of $MAPbI_3$ with MoS_2 nanosheets (MoS_2 NSs), resulting in a hybrid photocatalyst with high efficiency for visible-light-driven photocatalytic HER.[123] The composite exhibited excellent HER performance with an HER rate of 206.1 μmol h^{-1} (105 mg), which was a 121-fold enhancement compared to that of bare $MAPbI_3$. In addition, Zhang *et al.* fabricated a series of $MA_{1-x}FA_xPbI_3$ by partially replacing MA^+ with FA^+, which was then coupled with MoS_2 cocatalyst for photocatalytic HER. The optimized MoS_2/$MA_{0.6}FA_{0.4}PbI_3$ composite (*i.e.*, 20 wt% MoS_2/$MA_{0.6}FA_{0.4}PbI_3$) exhibited a superior 66.4 μmol h^{-1} (50 mg) visible HER rate, which was approximately 88-fold enhancement compared to that of pristine $MAPbI_3$ (1.2 μmol h^{-1}, 50 mg). The outstanding photocatalytic HER performances of MoS_2/$MA_{0.6}FA_{0.4}PbI_3$ could be attributed to the prolonged lifetime of photoinduced carriers inside $MA_{0.6}FA_{0.4}PbI_3$ due to the partial replacement of MA^+ with FA^+, and the enhanced carrier transfer and separation capabilities by MoS_2 decoration.

Subsequently, Zhao *et al.* developed a novel II-type heterojunction composite photocatalyst (Fig. 10b), consisting of monolayer MoS_2 nanosheets (ML-MoS_2) and $MAPbI_3$ microcrystals ($MAPbI_3$-MCs) (Fig. 10c), which could effectively inhibit carriers recombination for high-efficiency photocatalytic HER.[126] This discovery developed new possibilities for enhancing the HER performance of perovskite-based photocatalysts, achieving a remarkable STH efficiency of 1.09% and an HER rate of 1360 μmol h^{-1} (100 mg) under visible light. Furthermore, when other MHP microcrystals such as δ-$FAPbI_3$-MCs, $MASnI_3$-MCs, and $MA_3Bi_2I_9$-MCs were combined with ML-MoS_2 nanosheets, their HER rates increased by 8.4, 14.4, and 26 times, respectively, compared to their respective bare perovskite microcrystals. This indicates a hopeful approach for promoting the photocatalytic HER performance of halide perovskites. To further increase the active area of MoS_2, Guan *et al.* fabricated a MoS_2 nanoflowers/$MAPbI_3$ microcrystals heterostructure (Fig. 10d),[131] The MoS_2 edges offered large amounts of unsaturated S_2^{2-} that could be considered as active sites for HER.[163,164] Specifically, $MAPbI_3$/MoS_2 (3 : 7) exhibited a drastic enhancement in the HER rate, reaching up to 1469.45 μmol h^{-1} (50 mg) and a champion STH efficiency of 7.35%. Based on available research, this is one of the highest STHs in photocatalytic HER. Furthermore, Zhang *et al.* fabricated an I-type heterostructured MoS_2/$Cs_2AgBiBr_6$ for efficient and enduring photocatalytic HER *via* loading MoS_2 on $Cs_2AgBiBr_6$ using a dissolution–recrystallization method.[134] The optimized MoS_2/$Cs_2AgBiBr_6$ composite achieved an HER rate of 4.375 μmol h^{-1} (50 mg) in aqueous HBr solution, approximately 20-fold enhancement compared to that of bare $Cs_2AgBiBr_6$ (0.215 μmol h^{-1}, 50 mg), and presented an intermittent 500 h photocatalytic HER stability without obvious decrease. The enhanced activity of MoS_2/$Cs_2AgBiBr_6$ could be attributed to the kinetics-facilitated heterostructure consisting of stable $Cs_2AgBiBr_6$ and MoS_2.

4.3.3 Graphitic carbon nitride. $g\text{-}C_3N_4$ is a promising photocatalyst due to its high surface area, excellent interfacial charge separation and transport capability, and easy preparation, which is expected to integrate with MHPs with high light absorption ability.[165–168] Bresolin *et al.* first fabricated a $Cs_3Bi_2I_9/g\text{-}C_3N_4$ composite photocatalyst *via* anchoring $Cs_3Bi_2I_9$ perovskite on $g\text{-}C_3N_4$ nanosheets.[120] This composite was tested in a methanol solution (10 vol% in water) with an HER rate of 5.52 μmol h^{-1} (6 mg), which was approximately 46% higher than that of bare $g\text{-}C_3N_4$. The improved photocatalytic performance was attributed to the enhanced light absorption and electrochemical properties of the newly designed composite. Romani *et al.* synthesized water-insoluble $DMASnBr_3/g\text{-}C_3N_4$ heterostructures for photocatalytic HER in a 10 vol% triethanolamine (TEOA) solution (Fig. 10e).[128] The HER rate of the optimized $g\text{-}C_3N_4@DMASnBr_3/Pt$ heterostructure (36.33 μmol h^{-1}, 21 mg) was more than 288-fold higher than that of $Pt/DMASnBr_3$ and 100-fold better than that of bare $g\text{-}C_3N_4$. This excellent photocatalytic HER performance could be attributed to the good band alignment of $g\text{-}C_3N_4/DMASnBr_3$, which effectively enhance the separation of photogenerated carriers. The researchers also developed a heterostructured photocatalyst by combining $Cs_3Bi_2Br_9$ with $g\text{-}C_3N_4$.[130] Photocatalytic HER was performed in a 10 vol% aqueous TEOA with Pt as the cocatalyst. The optimal photocatalytic HER rate was achieved when the loading of $Cs_3Bi_2Br_9$ was 2.5%, reaching approximately 22.05 μmol h^{-1} (21 mg), which was about an order of magnitude better than that of bare $g\text{-}C_3N_4$ (1.701 μmol h^{-1}, 21 mg). However, when the $Cs_3Bi_2Br_9$ loading amount exceeded 5%, the HER capacity of the composite photocatalyst decreased, probably due to the self-trapping of the photogenerated electrons.

Additionally, Song *et al.* synthesized mesoporous $g\text{-}C_3N_4$ and then loaded it onto the surface of $Cs_2AgBiBr_6$.[136] High-resolution transmission electron microscope (HRTEM) images clearly showed the secure contact between $Cs_2AgBiBr_6$ and $g\text{-}C_3N_4$. Spectroscopy analysis indicated the establishment of a II-type heterojunction structure between $Cs_2AgBiBr_6$ and $g\text{-}C_3N_4$. The optimized $g\text{-}C_3N_4/Cs_2AgBiBr_6\text{-}10$ (with a mass ratio of $g\text{-}C_3N_4$ and $Cs_2AgBiBr_6$ being 1 : 10) exhibited an excellent photocatalytic HER rate of 3 μmol h^{-1} (50 mg) without using any noble metal cocatalyst, achieving a 2.5-fold enhancement compared to that of the original $Cs_2AgBiBr_6$. Moreover, its photocatalytic HER efficiency showed no obvious decrease after storage for 40 days in air condition, indicating excellent stability and photocatalytic recyclability. Jiang *et al.* utilized a nitrogen-doped carbon (N-C) material based on $g\text{-}C_3N_4$ and coupled it with $Cs_2AgBiBr_6$ *via* a facile hydrothermal method.[132,169] The photocatalytic HER performance test found that N-C itself had no photocatalytic HER ability. After combining with $Cs_2AgBiBr_6$, the composite material exhibited good photocatalytic HER activity. Particularly, when tested a hydrothermal temperature of 140 °C, $Cs_2AgBiBr_6$/N-C-140 exhibited the best HER rate of 3.8 μmol h^{-1} (10 mg), about 19 times that of the bare $Cs_2AgBiBr_6$. This improvement was ascribed to the large surface area of N-C and the presence of nitrogen atoms in N-C, which enhanced electron conductivity and promoted interfacial charge separation between $Cs_2AgBiBr_6$ and N-C.

4.3.4 Black phosphorous. Black phosphorus (BP) with high charge carrier mobility and abundant active sites has also been introduced to improve light absorption and photoinduced carriers separation of MHPs.[170,171] For example, Li *et al.* reported a $BP/MAPbI_3$ heterostructure.[116] Under solar-light irradiation, the photogenerated electrons could transfer from perovskite $MAPbI_3$ to BP to participate in the HER. Interestingly, the HER rate of the $BP/MAPbI_3$ heterostructure (112.26 μmol h^{-1}, 30 mg) was more than 100-fold enhancement compared to that of bare $MAPbI_3$. This outstanding photocatalytic HER activity could be ascribed to the construction of a type I heterojunction, which could broaden light harvesting and enhance the separation and migration of carriers at the interface of $BP/MAPbI_3$.

4.3.5 Lamellar transition metal borides. Jiang *et al.* developed a $NiCoB/MAPbI_3$ composite photocatalyst by combining amorphous NiCoB with a nanoscale lamellar structure, and $MAPbI_3$ using electrostatic self-assembly.[129] The photogenerated electrons from $MAPbI_3$ were able to transfer to NiCoB and participate in the reduction of H^+, thereby promoting the separation of photoinduced carriers. At a NiCoB loading of 30%, the photocatalytic HER rate of $MAPbI_3$ reached a maximum of 170.7 μmol h^{-1} (65 mg) under visible light irradiation. Additionally, the composite showed good stability in a 24-hour cycling photocatalytic HER.

4.4 Metal halide perovskite/1D semiconductor composites

Conductive 1D polyaniline nanowires (PANI NWs) with high electrical conductivity and excellent chemical stability have been coupled with MHP to create high-performance composite photocatalysts. For example, Li *et al.* fabricated a high-performance 3D/1D heterostructured composite photocatalyst by combining conductive 1D polyaniline nanowires (PANI NWs) with $MAPbI_3$ using an *in situ* doping-induced assembly method.[133] SEM images obtained by Li *et al.* showed that PANI NWs were firmly embedded on the surface of $MAPbI_3$. The $MAPbI_3$/PANI NWs composite photocatalyst showed a remarkable 29-fold increase in the photocatalytic HER rate (38.8 μmol h^{-1}, 107 mg) compared to that of pristine $MAPbI_3$ microcrystals. Additionally, this composite photocatalyst demonstrated good stability during 30 h of irradiation, with each cycle lasting 6 h.

4.5 Metal halide perovskite/other material composites

In addition to the aforementioned materials, other semiconductors have also been used to couple with MHPs to create efficient photocatalytic systems. One such material is metal–organic frameworks (MOFs), which possess a large specific surface area, adjustable morphology, and diverse structure.[172,173] By coupling MOFs with MHPs, the photocatalytic HER performance of MHPs can be enhanced. For instance, Feng *et al.* fabricated a $CsPbBr_3$/zeolitic imidazolate framework

(ZIF-8) composite using the mechanical milling method. This fabrication method was expected to enable large-scale synthesis of ZIF-8 composites (Fig. 10f).[135] SEM images showed that ZIF-8 was loaded on the surface of $CsPbBr_3$. The HER rate of this composite was measured to be ∼11 times higher (2.36 μmol·h^{-1}, 300 mg, 2.5 h) than that of ZIF-8 alone (0.205 μmol·h^{-1}, 300 mg, 2.5 h), benefiting from the ZIF-8 promoted photogenerated carrier separation. Moreover, ZIF-8 was discerned to enhance the stability of $CsPbBr_3$ in aqueous solution, with only ∼8% decrease in H_2 productivity after 4 weeks.

In addition to the above-mentioned strategies, the formation of MHP-MHPs heterojunctions has also been demonstrated as an effective approach to obtaining high-performance photocatalytic systems. For example, Tang *et al.* developed a lead-free Bi-based hybrid perovskite heterojunction, $MA_3Bi_2I_9$/DMA_3BiI_6, through an *in situ* growth method.[124] The VB and CB positions of $MA_3Bi_2I_9$ and DMA_3BiI_6 showed a well-matched II-type heterostructure, which facilitates the formation of an interfacial carriers transfer pathway at the interface of $MA_3Bi_2I_9$ and DMA_3BiI_6. This resulted in an HER rate of 39.64 μmol h^{-1} (200 mg) without the addition of Pt co-catalysts.

5. Summary and prospects

MHPs have garnered significant interest in the field of photocatalytic H_2 evolution due to their outstanding photoelectric properties and tunable crystal structure. This review comprehensively discusses the structure and photocatalytic HER performance of different kinds of MHPs, including both lead-based perovskites and lead-free perovskites. Additionally, we summarize the developed strategies used to improve the photocatalytic performance of MHPs, including energy band structure adjustment (*e.g.*, extra halogen element doping), and composite structures (*e.g.*, MHPs/conductor, MHPs/semiconductor). However, despite their potential, the current photocatalytic performance of MHPs remains unsatisfactory for practical application, due to energy loss during charge generation, separation, and transfer, as well as concerns about the instability and toxicity of MHPs. In light of current MHP research, we propose several possible methods to further enhance the photocatalytic performance of MHP-based photocatalysts.

(1) Designing MHPs with optimal intrinsic crystalline structures at the molecular level. Photocatalysts play a crucial role in photocatalytic reactions, encompassing light absorption, photogenerated carriers generation, separation, transport, and surface redox reactions. To achieve efficient H_2 evolution, photocatalysts require appropriate electronic structures, wide light absorption range, large absorption coefficients, and excellent carrier transport performance.[174] The strong structural diversity and designability of MHPs make them highly advantageous for the design of photocatalysts. Emphatically, incorporating bulky organic cations at the A site can improve the intrinsic moisture resistance of MHPs, owing to the hydrophobic nature of the organic cations. However, introducing bulky organic cations may cause the breakdown of the 3D perovskite framework, leading to the formation of low-dimensional perovskites such as 2D, 1D, and 0D perovskites. These low-dimensional perovskites, especially 1D and 0D perovskites, usually exhibit stronger quantum confinement effects and wider bandgaps compared to their 3D analogues, which may impair their optoelectronic properties.[65] Thus, striking a balance between optoelectronic performance and stability in MHPs design is of utmost importance. For instance, quasi-2D MHPs with a general formula of $A_2A_{n-1}{}'Pb_nI_{3n+1}$, (where A′ is a bulky organic cation and A is MA or FA) have demonstrated higher environmental stability compared with $MAPbI_3$, due to the protection of the hydrophobic organic spacers. In particular, solar cells based on quasi-2D MHPs have recently achieved a remarkable power conversion efficiency (PCE) of 22.26%, indicating the preserved excellent semiconducting properties of these materials.[175] Further theoretical calculations and molecular engineering hold promise in promoting the development of MHPs for efficient and stable photocatalytic HER.

(2) Constructing band-matched heterostructured MHP composites. Although some strategies have achieved improved carrier separation efficiency, they often come at the expense of redox ability, ultimately leading to unsatisfactory photocatalytic HER performance. Additionally, the existence of photo-induced electron–hole pairs in the pristine photocatalyst may hinder the efficient interfacial transfer of electron–hole pairs in other catalysts. To overcome these limitations and further improve the photocatalytic HER performance of MHPs, novel forms of heterostructures, such as Z- and S-scheme heterojunctions, are expected.[139,176] By selectively consuming or recombining a certain portion of photogenerated electrons and holes, electrons and holes with stronger redox ability can be retained, thus enhancing the photocatalytic activity of these heterojunctions. Moreover, it is important to consider the condition under which most MHPs-based photocatalytic HERs are realized, often using a HI solution. Thus, selecting a suitable acid-resistant photocatalyst for oxygen evolution based on the I^-/I_3^- redox pair is expected to improve the efficiency of the photocatalytic HER process and enable overall water splitting.

(3) Developing encapsulation layers. Encapsulation is a crucial step in improving the stability of photocatalytic plate devices, as the water-instability of MHPs presents a significant challenge in the context of photocatalytic H_2 production. An ideal encapsulation material should possess excellent stability, good electrical conductivity, and light transmission. There are generally two types of encapsulations: full coverage and edge encapsulation. Full coverage encapsulation involves preparing the encapsulation layer on top of the module, while edge encapsulation involves placing a sealant around the module.[177–179] Edge encapsulation offers advantages such as reduced impact on the contact layer, lowered light transmission requirements, and minimized potential side reactions between the encapsulating materials and the MHPs. However, the encapsulation effect may be slightly reduced compared to full coverage encapsulation. To further increase the barrier effect, desiccant can be introduced into the edge encapsulation process. Fully covered encapsulation

provides better protection, but it has a greater impact on the MHP layer and has higher light transmission requirements, as it directly contacts the MHP functional layer. An alternative approach involves multilayer encapsulation, which combines the benefits of both full coverage and edge encapsulation methods to improve the water stability of MHPs while maintaining their photocatalytic activity.[180] However, it is important to note that this method is may be challenging to fabricate and could incur higher expensive.

(4) Developing lead-free MHP photocatalysts. Among the candidates, Sn-based perovskites have shown promise due to the similarity of Sn^{2+} to Pb^{2+} in terms of electron configuration and ionic radius. However, the rapid oxidation of Sn^{2+} to Sn^{4+} remains a challenge. Various stabilization methods have been explored, such as adding reducing agents (*e.g.* H_3PO_2),[181] but their stability remains inferior to Pb-based perovskites. A deeper understanding of Sn^{2+} bonding interactions in Sn-based perovskites could offer insights into addressing this issue. Similarly, Ge-based perovskites also face the challenge of Ge^{2+} oxidation. Bi-, Sb-based perovskites and double perovskites have demonstrated good stability under various conditions. However, their photocatalytic performance is generally limited by poor optoelectronic properties arising from their low electronic dimensional.[182] Therefore, a promising direction for MHP-based photocatalytic H_2 evolution is the rational design of Bi-, Sb-based perovskites and double perovskites with high electronic dimensional using theoretical calculations and molecular engineering.

Conflicts of interest

There are no conflicts to declare.

Acknowledgements

This work was financially supported by National Ten Thousand Talent Program for Young Top-notch Talent, National Natural Science Fund for Excellent Young Scholars (52022030), National Natural Science Foundation of China (51972111, 52203330), the Science and Technology Innovation Plan of Shanghai Science and Technology Commission (22YF1410000), Shanghai Pilot Program for Basic Research (22TQ1400100-5), ''Dawn'' Program of Shanghai Education Commission (22SG28), Shanghai Municipal Natural Science Foundation (22ZR1418000), Postdoctoral Research Foundation of China (2021M701190) and Shanghai Engineering Research Center of Hierarchical Nanomaterials (18DZ2252400).

Notes and references

1 J. Sun, D. K. Zhong and D. R. Gamelin, Composite photoanodes for photoelectrochemical solar water splitting, *Energy Environ. Sci.*, 2010, **3**, 1252–1261.

2 J. Song, T. L. Kim, J. Lee, S. Y. Cho, J. Cha, S. Y. Jeong, H. An, W. S. Kim, Y.-S. Jung, J. Park, G. Y. Jung, D.-Y. Kim, J. Y. Jo, S. D. Bu, H. W. Jang and S. Lee, Domain-engineered $BiFeO_3$ thin-film photoanodes for highly enhanced ferroelectric solar water splitting, *Nano Res.*, 2018, **11**, 642–655.

3 J. Liu, Y. Liu, N. Y. Liu, Y. Z. Han, X. Zhang, H. Huang, Y. Lifshitz, S. T. Lee, J. Zhong and Z. H. Kang, Metal-free efficient photocatalyst for stable visible water splitting *via* a two-electron pathway, *Science*, 2015, **347**, 970–974.

4 Y. O. Wang, A. Vogel, M. Sachs, R. S. Sprick, L. Wilbraham, S. J. A. Moniz, R. Godin, M. A. Zwijnenburg, J. R. Durrant, A. I. Cooper and J. W. Tang, Current understanding and challenges of solar-driven hydrogen generation using polymeric photocatalysts, *Nat. Energy*, 2020, **5**, 633.

5 W. Bi, X. Li, L. Zhang, T. Jin, L. Zhang, Q. Zhang, Y. Luo, C. Wu and Y. Xie, Molecular co-catalyst accelerating hole transfer for enhanced photocatalytic H_2 evolution, *Nat. Commun.*, 2015, **6**, 8647.

6 M. Z. Jacobson, W. G. Colella and D. M. Golden, Cleaning the air and improving health with hydrogen fuel-cell vehicles, *Science*, 2005, **308**, 1901–1905.

7 J. Pan, Y. Sun, W. Li, J. Knight and A. Manthiram, A green lead hydrometallurgical process based on a hydrogen-lead oxide fuel cell, *Nat. Commun.*, 2013, **4**, 2178.

8 Y. Yang, X. He, P. Zhang, Y. H. Andaloussi, H. Zhang, Z. Jiang, Y. Chen, S. Ma, P. Cheng and Z. Zhang, Combined intrinsic and extrinsic proton conduction in robust covalent organic frameworks for hydrogen fuel cell applications, *Angew. Chem., Int. Ed.*, 2020, **59**, 3678–3684.

9 S. Manigandan, R. Sarweswaran, P. B. Devi, Y. Sohret, A. Kondratiev, S. Venkatesh, M. R. Vimal and J. J. Joshua, Comparative study of nanoadditives TiO_2, CNT, Al_2O_3, CuO and CeO_2 on reduction of diesel engine emission operating on hydrogen fuel blends, *Fuel*, 2020, **262**, 116336.

10 C. Gong, Z. Li, J. Sun and F. Liu, Evaluation on combustion and lean-burn limit of a medium compression ratio hydrogen/methanol dual-injection spark-ignition engine under methanol late-injection, *Appl. Energy*, 2020, **277**, 115622.

11 C. Acar and I. Dincer, The potential role of hydrogen as a sustainable transportation fuel to combat global warming, *Int. J. Hydrogen Energy*, 2020, **45**, 3396–3406.

12 J. Zhong, X. Yang, Z. Wu, B. Liang, Y. Huang and T. Zhang, State of the art and perspectives in heterogeneous catalysis of CO_2 hydrogenation to methanol, *Chem. Soc. Rev.*, 2020, **49**, 1385–1413.

13 C. Mao, J. Wang, Y. Zou, G. Qi, J. Y. Yang Loh, T. Zhang, M. Xia, J. Xu, F. Deng, M. Ghoussoub, N. P. Kherani, L. Wang, H. Shang, M. Li, J. Li, X. Liu, Z. Ai, G. A. Ozin, J. Zhao and L. Zhang, Hydrogen spillover to oxygen vacancy of $TiO_{2-x}H_y$/Fe: Breaking the scaling relationship of ammonia synthesis, *J. Am. Chem. Soc.*, 2020, **142**, 17403–17412.

14 D. Wu, K. Deng, B. Hu, Q. Lu, G. Liu and X. Hong, Plasmon-assisted photothermal catalysis of low-pressure CO_2 hydrogenation to methanol over Pd/ZnO catalyst, *ChemCatChem*, 2019, **11**, 1598–1601.

15 Q. Xiang, J. Yu and M. Jaroniec, Synergetic effect of MoS_2 and graphene as cocatalysts for enhanced photocatalytic

H_2 production activity of TiO_2 nanoparticles, *J. Am. Chem. Soc.*, 2012, **134**, 6575–6578.

16 J. Ran, J. Zhang, J. Yu, M. Jaroniec and S. Z. Qiao, Earth-abundant cocatalysts for semiconductor-based photocatalytic water splitting, *Chem. Soc. Rev.*, 2014, **43**, 7787–7812.

17 Q. Lu, Y. Yu, Q. Ma, B. Chen and H. Zhang, 2D transition-metal-dichalcogenide-nanosheet-based composites for photocatalytic and electrocatalytic hydrogen evolution reactions, *Adv. Mater.*, 2016, **28**, 1917–1933.

18 M. Zhu, Z. Sun, M. Fujitsuka and T. Majima, Z-scheme photocatalytic water splitting on a 2D heterostructure of black phosphorus/bismuth vanadate using visible light, *Angew. Chem., Int. Ed.*, 2018, **57**, 2160–2164.

19 Q. Guo, Z. Ma, C. Zhou, Z. Ren and X. Yang, Single molecule photocatalysis on TiO_2 surfaces, *Chem. Rev.*, 2019, **119**, 11020–11041.

20 S. Jayachitra, D. Mahendiran, P. Ravi, P. Murugan and M. Sathish, Highly conductive $NiSe_2$ nanoparticle as a co-catalyst over TiO_2 for enhanced photocatalytic hydrogen production, *Appl. Catal., B*, 2022, **307**, 121159.

21 H. G. Yang, C. H. Sun, S. Z. Qiao, J. Zou, G. Liu, S. C. Smith, H. M. Cheng and G. Q. Lu, Anatase TiO_2 single crystals with a large percentage of reactive facets, *Nature*, 2008, **453**, 638–641.

22 Q. Sun, N. Wang, J. Yu and J. C. Yu, A hollow porous CdS photocatalyst, *Adv. Mater.*, 2018, **30**, 1804368.

23 H. Ren, J.-L. Yang, W.-M. Yang, H.-L. Zhong, J.-S. Lin, P. M. Radjenovic, L. Sun, H. Zhang, J. Xu, Z.-Q. Tian and J.-F. Li, Core–shell–satellite plasmonic photocatalyst for broad-spectrum photocatalytic water splitting, *ACS Mater. Lett.*, 2021, **3**, 69–76.

24 C.-Q. Li, X. Du, S. Jiang, Y. Liu, Z.-L. Niu, Z.-Y. Liu, S.-S. Yi and X.-Z. Yue, Constructing direct Z-scheme heterostructure by enwrapping $ZnIn_2S_4$ on CdS hollow cube for efficient photocatalytic H_2 generation, *Adv. Sci.*, 2022, **9**, 2201773.

25 L. Mu, Y. Zhao, A. Li, S. Wang, Z. Wang, J. Yang, Y. Wang, T. Liu, R. Chen, J. Zhu, F. Fan, R. Li and C. Li, Enhancing charge separation on high symmetry $SrTiO_3$ exposed with anisotropic facets for photocatalytic water splitting, *Energy Environ. Sci.*, 2016, **9**, 2463–2469.

26 C. M. Pelicano, M. Saruyama, R. Takahata, R. Sato, Y. Kitahama, H. Matsuzaki, T. Yamada, T. Hisatomi, K. Domen and T. Teranishi, Bimetallic synergy in ultrafine cocatalyst alloy nanoparticles for efficient photocatalytic water splitting, *Adv. Funct. Mater.*, 2022, **32**, 2202987.

27 J. Pan, Z. Chen, P. Wang, P. Wang, Q. Yu, W. Zhao, J. Wang, M. Zhu, Y. Zheng and C. Li, The overall water splitting of CdS/Ti^{3+}-$SrTiO_3$ core–shell heterojunction *via* OER enhancement of MnO_x nanoparticles, *Chem. Eng. J.*, 2021, **424**, 130357.

28 Q. Liu, J. Shen, X. Yu, X. Yang, W. Liu, J. Yang, H. Tang, H. Xu, H. Li, Y. Li and J. Xu, Unveiling the origin of boosted photocatalytic hydrogen evolution in simultaneously (S, P, O)-codoped and exfoliated ultrathin g-C_3N_4 nanosheets, *Appl. Catal., B*, 2019, **248**, 84–94.

29 C. Hu, F. Chen, Y. Wang, N. Tian, T. Ma, Y. Zhang and H. Huang, Exceptional cocatalyst-free photo-enhanced piezocatalytic hydrogen evolution of carbon nitride nanosheets from strong in-plane polarization, *Adv. Mater.*, 2021, **33**, 2101751.

30 Z. Wang, Z. Wang, X. Zhu, C. Ai, Y. Zeng, W. Shi, X. Zhang, H. Zhang, H. Si, J. Li, C.-Z. Wang and S. Lin, Photodepositing CdS on the active cyano groups decorated g-C_3N_4 in Z-scheme manner promotes visible-light-driven hydrogen evolution, *Small*, 2021, **17**, 2102699.

31 Y. Liu, B. Dong, A. Hagfeldt, J. Luo and M. Graetzel, Chemically tailored molecular surface modifiers for efficient and stable perovskite photovoltaics, *SmartMat*, 2021, **2**, 33–37.

32 Y. Peng, X. Wang, L. Li, H. Ye, S. Yang, H. G. Yang, J. Luo and Y. Hou, Moisture-resistant chiral perovskites for white-light circularly polarized photoluminescence, *Adv. Opt. Mater.*, 2023, **11**, 2201888.

33 C. Zou, Z. Zhou, X. Liu, F. Zhang, J. Xie, Y. Su, S. Yang and Y. Hou, Multication tin-lead perovskite photodiodes with engineered lattice strain for ultrasensitive broadband photodetection, *Adv. Opt. Mater.*, 2022, **10**, 2201769.

34 Y. Yin, Z. Guo, G. Chen, H. Zhang and W.-J. Yin, Recent progress in defect tolerance and defect passivation in halide perovskite solar cells, *Acta Phys. Chim. Sin.*, 2021, **4**, 2008048.

35 Y.-H. Zhang and Y. Li, Interface materials for perovskite solar cells, *Rare Met.*, 2021, **40**, 2993–3018.

36 Q. Li, Y. Zheng, Z. Wei, J. Xie, C. Zou, X. Liu, D. Liu, Z. Zhou, H. G. Yang, S. Yang and Y. Hou, Halide diffusion equilibrium and its impact on efficiency evolution of perovskite solar cells, *Adv. Energy Mater.*, 2022, **12**, 2202982.

37 Y. Shi, J. He, H. Lian, X. Liu, H. Yuan, Y. Hou, S. Yang and H. G. Yang, Cooperative adsorption of metal-organic complexes on $CsPbI_2Br$ perovskite surface for photovoltaic efficiency exceeding 17%, *ChemSusChem*, 2022, **15**, e202201394.

38 Z. Yuan, Z. Hu, I. Persson, C. Wang, X. Liu, C. Kuang, W. Xu, S. Bai and F. Gao, Interface-assisted cation exchange enables high-performance perovskiteLEDs with tunable near-infrared emissions, *Joule*, 2022, **6**, 2423–2436.

39 C. Zhang, S. Wang, X. Li, M. Yuan, L. Turyanska and X. Yang, Core/shell perovskite nanocrystals: Synthesis of highly efficient and environmentally stable $FAPbBr_3$/$CsPbBr_3$ for LED applications, *Adv. Funct. Mater.*, 2020, **30**, 1910582.

40 E.-P. Yao, Z. Yang, L. Meng, P. Sun, S. Dong, Y. Yang and Y. Yang, High-brightness blue and white LEDs based on inorganic perovskite nanocrystals and their composites, *Adv. Mater.*, 2017, **29**, 1606859.

41 D. H. Chun, Y. J. Choi, Y. In, J. K. Nam, Y. J. Choi, S. Yun, W. Kim, D. Choi, D. Kim, H. Shin, J. H. Cho and J. H. Park, Halide perovskite nanopillar photodetector, *ACS Nano*, 2018, **12**, 8564–8571.

42 L. Martínez-Goyeneche, L. Gil-Escrig, I. Susic, D. Tordera, H. J. Bolink and M. Sessolo, Narrowband monolithic

perovskite–perovskite tandem photodetectors, *Adv. Opt. Mater.*, 2022, **10**, 2201047.

43 W. Tian, H. Zhou and L. Li, Hybrid organic–inorganic perovskite photodetectors, *Small*, 2017, **13**, 1702107.

44 J. Park, J. Kim, H.-S. Yun, M. J. Paik, E. Noh, H. J. Mun, M. G. Kim, T. J. Shin and S. I. Seok, Controlled growth of perovskite layers with volatile alkylammonium chlorides, *Nature*, 2023, **616**, 724–730.

45 S. Sun, T. Salim, N. Mathews, M. Duchamp, C. Boothroyd, G. Xing, T. C. Sum and Y. M. Lam, The origin of high efficiency in low-temperature solution-processable bilayer organometal halide hybrid solar cells, *Energy Environ. Sci.*, 2014, **7**, 399–407.

46 N.-G. Park, Perovskite solar cells: an emerging photovoltaic technology, *Mater. Today*, 2015, **18**, 65–72.

47 W. Zhang, M. Saliba, S. D. Stranks, Y. Sun, X. Shi, U. Wiesner and H. J. Snaith, Enhancement of perovskite-based solar cells employing core–shell metal nanoparticles, *Nano Lett.*, 2013, **13**, 4505–4510.

48 V. D'Innocenzo, G. Grancini, M. J. P. Alcocer, A. R. S. Kandada, S. D. Stranks, M. M. Lee, G. Lanzani, H. J. Snaith and A. Petrozza, Excitons versus free charges in organo-lead tri-halide perovskites, *Nat. Commun.*, 2014, **5**, 3586.

49 C. Zhou, Q. Ou, W. Chen, Z. Gan, J. Wang, Q. Bao, X. Wen and B. Jia, Illumination-induced halide segregation in gradient bandgap mixed-halide perovskite nanoplatelets, *Adv. Opt. Mater.*, 2018, **6**, 1801107.

50 W. Zhou, P. Han, X. Zhang, D. Zheng, S. Yang, Y. Yang, C. Luo, B. Yang, F. Hong, D. Wei, R. Lu and K. Han, Lead-free small-bandgap $Cs_2CuSbCl_6$ double perovskite nanocrystals, *J. Phys. Chem. Lett.*, 2020, **11**, 6463–6467.

51 S. Purohit, K. L. Yadav and S. Satapathi, Metal halide perovskite heterojunction for photocatalytic hydrogen generation: Progress and future opportunities, *Adv. Mater. Interfaces*, 2022, **9**, 2200058.

52 K. Ren, S. Yue, C. Li, Z. Fang, K. A. M. Gasem, J. Leszczynski, S. Qu, Z. Wang and M. Fan, Metal halide perovskites for photocatalysis applications, *J. Mater. Chem. A*, 2022, **10**, 407–429.

53 B.-M. Bresolin, Y. Park and D. W. Bahnemann, Recent progresses on metal halide perovskite-based material as potential photocatalyst, *Catalysts*, 2020, **10**, 709.

54 G. E. Eperon, G. M. Paternò, R. J. Sutton, A. Zampetti, A. A. Haghighirad, F. Cacialli and H. J. Snaith, Inorganic caesium lead iodide perovskite solar cells, *J. Mater. Chem. A*, 2015, **3**, 19688–19695.

55 Y. Zhao and K. Zhu, Organic–inorganic hybrid lead halide perovskites for optoelectronic and electronic applications, *Chem. Soc. Rev.*, 2016, **45**, 655–689.

56 Y. Liu, Z. Yang and S. Liu, Recent progress in single-crystalline perovskite research including crystal preparation, property evaluation, and applications, *Adv. Sci.*, 2018, **5**, 1700471.

57 C. Zhou, H. Lin, S. Lee, M. Chaaban and B. Ma, Organic–inorganic metal halide hybrids beyond perovskites, *Mater. Res. Lett.*, 2018, **6**, 552–569.

58 W. Wu, X. Shang, Z. Xu, H. Ye, Y. Yao, X. Chen, M. Hong, J. Luo and L. Li, Toward efficient two-photon circularly polarized light detection through cooperative strategies in chiral quasi-2D perovskites, *Adv. Sci.*, 2023, **10**, 2206070.

59 C. M. M. Soe, C. C. Stoumpos, M. Kepenekian, B. Traoré, H. Tsai, W. Nie, B. Wang, C. Katan, R. Seshadri, A. D. Mohite, J. Even, T. J. Marks and M. G. Kanatzidis, New type of 2D perovskites with alternating cations in the interlayer space, $(C(NH_2)_3)(CH_3NH_3)_nPb_nI_{3n+1}$: Structure, properties, and photovoltaic performance, *J. Am. Chem. Soc.*, 2017, **139**, 16297–16309.

60 Z. Yuan, C. Zhou, Y. Tian, Y. Shu, J. Messier, J. C. Wang, L. J. van de Burgt, K. Kountouriotis, Y. Xin, E. Holt, K. Schanze, R. Clark, T. Siegrist and B. Ma, One-dimensional organic lead halide perovskites with efficient bluish white-light emission, *Nat. Commun.*, 2017, **8**, 14051.

61 L.-J. Feng, Y.-Y. Zhao, R.-Y. Song and X.-W. Lei, Three homologous 1D lead halide perovskites with broadband white-light emissions, *Inorg. Chem. Commun.*, 2022, **136**, 109146.

62 C. Zhou, H. Lin, H. Shi, Y. Tian, C. Pak, M. Shatruk, Y. Zhou, P. Djurovich, M.-H. Du and B. Ma, A Zero-dimensional organic seesaw-shaped tin bromide with highly efficient strongly Stokes-shifted deep-red emission, *Angew. Chem., Int. Ed.*, 2018, **57**, 1021–1024.

63 C. Zhou, Y. Tian, M. Wang, A. Rose, T. Besara, N. K. Doyle, Z. Yuan, J. C. Wang, R. Clark, Y. Hu, T. Siegrist, S. Lin and B. Ma, Low-dimensional organic tin bromide perovskites and their photoinduced structural transformation, *Angew. Chem., Int. Ed.*, 2017, **56**, 9018–9022.

64 Z. Xiao, W. Meng, J. Wang, D. B. Mitzi and Y. Yan, Searching for promising new perovskite-based photovoltaic absorbers: the importance of electronic dimensionality, *Mater. Horizons*, 2017, **4**, 206–216.

65 S. A. Kulkarni, N. Yantara, K. S. Tan, N. Mathews and S. G. Mhaisalkar, Perovskite nanostructures: Leveraging quantum effects to challenge optoelectronic limits, *Mater. Today*, 2020, **33**, 122–140.

66 Y. Peng, X. Liu, L. Li, Y. Yao, H. Ye, X. Shang, X. Chen and J. Luo, Realization of vis–NIR dual-modal circularly polarized light detection in chiral perovskite bulk crystals, *J. Am. Chem. Soc.*, 2021, **143**, 14077–14082.

67 Y. Ai, X.-G. Chen, P.-P. Shi, Y.-Y. Tang, P.-F. Li, W.-Q. Liao and R.-G. Xiong, Fluorine substitution induced high T_c of enantiomeric perovskite ferroelectrics: (*R*)- and (*S*)-3-(Fluoropyrrolidinium)$MnCl_3$, *J. Am. Chem. Soc.*, 2019, **141**, 4474–4479.

68 Y. Gao, E. Shi, S. Deng, S. B. Shiring, J. M. Snaider, C. Liang, B. Yuan, R. Song, S. M. Janke, A. Liebman-Peláez, P. Yoo, M. Zeller, B. W. Boudouris, P. Liao, C. Zhu, V. Blum, Y. Yu, B. M. Savoie, L. Huang and L. Dou, Molecular engineering of organic–inorganic hybrid perovskites quantum wells, *Nat. Chem.*, 2019, **11**, 1151–1157.

69 Y. Gao, Z. Wei, S.-N. Hsu, B. W. Boudouris and L. Dou, Two-dimensional halide perovskites featuring semiconducting organic building blocks, *Mater. Chem. Front.*, 2020, **4**, 3400–3418.

70 Y. Peng, J. Bie, X. Liu, L. Li, S. Chen, W. Fa, S. Wang, Z. Sun and J. Luo, Acquiring high-T_C layered metal halide ferroelectrics *via* cage-confined ethylamine rotators, *Angew. Chem., Int. Ed.*, 2021, **60**, 2839–2843.
71 H.-Y. Liu, H.-Y. Zhang, X.-G. Chen and R.-G. Xiong, Molecular design principles for ferroelectrics: Ferroelectrochemistry, *J. Am. Chem. Soc.*, 2020, **142**, 15205–15218.
72 M. Shao, T. Bie, L. Yang, Y. Gao, X. Jin, F. He, N. Zheng, Y. Yu and X. Zhang, Over 21% efficiency stable 2D perovskite solar cells, *Adv. Mater.*, 2022, **34**, 2107211.
73 B. R. Wygant, A. Z. Ye, A. Dolocan, Q. Vu, D. M. Abbot and C. B. Mullins, Probing the degradation chemistry and enhanced stability of 2D organolead halide perovskites, *J. Am. Chem. Soc.*, 2019, **141**, 18170–18181.
74 R. K. Ulaganathan, R. C. Murugesan, C.-Y. Lin, A. Subramanian, W.-L. Chen, Y.-M. Chang, A. Rozhin and R. Sankar, Stable formamidinium-based centimeter long two-dimensional lead halide perovskite single-crystal for long-life optoelectronic applications, *Adv. Funct. Mater.*, 2022, **32**, 2112277.
75 S. Park, W. J. Chang, C. W. Lee, S. Park, H.-Y. Ahn and K. T. Nam, Photocatalytic hydrogen generation from hydriodic acid using methylammonium lead iodide in dynamic equilibrium with aqueous solution, *Nat. Energy*, 2016, **2**, 16185.
76 P. C. K. Vesborg, Photocatalysis: HI-time for perovskites, *Nat. Energy*, 2017, **2**, 16205.
77 C. Bie, L. Wang and J. Yu, Challenges for photocatalytic overall water splitting, *Chem*, 2022, **8**, 1567–1574.
78 J. Schneidewind, M. A. Argüello Cordero, H. Junge, S. Lochbrunner and M. Beller, Two-photon, visible light water splitting at a molecular ruthenium complex, *Energy Environ. Sci.*, 2021, **14**, 4427–4436.
79 C. Levy-Clement, A. Heller, W. A. Bonner and B. A. Parkinson, Spontaneous photoelectrolysis of HBr and HI, *J. Electrochem. Soc.*, 1982, **129**, 1701.
80 J. H. Norman, K. J. Mysels, R. Sharp and D. Williamson, Studies of the sulfur-iodine thermochemical water-splitting cycle, *Int. J. Hydrogen Energy*, 1982, **7**, 545–556.
81 H. Wang, H. Zhang, J. Wang, Y. Gao, F. Fan, K. Wu, X. Zong and C. Li, Mechanistic understanding of efficient photocatalytic H_2 evolution on two-dimensional layered lead iodide hybrid perovskites, *Angew. Chem., Int. Ed.*, 2021, **60**, 7376–7381.
82 Y. Li, L. Li, S. She, S. Chen, Y. Liu, B. Xu, F.-W. Lee and X. Zhu, Multidimensional perovskite for visible light driven hydrogen production in aqueous HI solution, *ACS Appl. Energy Mater.*, 2022, **5**, 207–213.
83 H. Huang, D. Verhaeghe, B. Weng, B. Ghosh, H. Zhang, J. Hofkens, J. A. Steele and M. B. J. Roeffaers, Metal halide perovskite based heterojunction photocatalysts, *Angew. Chem., Int. Ed.*, 2022, **61**, e202203261.
84 V. Armenise, S. Colella, F. Fracassi and A. Listorti, Lead-free metal halide perovskites for hydrogen evolution from aqueous solutions, *Nanomaterials*, 2021, **11**, 433.
85 Y. Wu, P. Wang, Z. Guan, J. Liu, Z. Wang, Z. Zheng, S. Jin, Y. Dai, M.-H. Whangbo and B. Huang, Enhancing the photocatalytic hydrogen evolution activity of mixed-halide perovskite $CH_3NH_3PbBr_{3-x}I_x$ achieved by bandgap funneling of charge carriers, *ACS Catal.*, 2018, **8**, 10349–10357.
86 H. Zhao, Y. Li, B. Zhang, T. Xu and C. Wang, PtI_x/$[(CH_3)_2NH_2]_3[BiI_6]$ as a well-dispersed photocatalyst for hydrogen production in hydroiodic acid, *Nano Energy*, 2018, **50**, 665–674.
87 D. Ju, X. Zheng, J. Liu, Y. Chen, J. Zhang, B. Cao, H. Xiao, O. F. Mohammed, O. M. Bakr and X. Tao, Reversible band gap narrowing of Sn-based hybrid perovskite single crystal with excellent phase stability, *Angew. Chem., Int. Ed.*, 2018, **57**, 14868–14872.
88 Z. Zhao, J. Wu, Y.-Z. Zheng, N. Li, X. Li, Z. Ye, S. Lu, X. Tao and C. Chen, Stable hybrid perovskite $MAPb(I_{1-x}Br_x)_3$ for photocatalytic hydrogen evolution, *Appl. Catal., B*, 2019, **253**, 41–48.
89 Z. Guan, Y. Wu, P. Wang, Q. Zhang, Z. Wang, Z. Zheng, Y. Liu, Y. Dai, M.-H. Whangbo and B. Huang, Perovskite photocatalyst $CsPbBr_{3-x}I_x$ with a bandgap funnel structure for H_2 evolution under visible light, *Appl. Catal., B*, 2019, **245**, 522–527.
90 M. Wang, Y. Zuo, J. Wang, Y. Wang, X. Shen, B. Qiu, L. Cai, F. Zhou, S. P. Lau and Y. Chai, Remarkably enhanced hydrogen generation of organolead halide perovskites *via* piezocatalysis and photocatalysis, *Adv. Energy Mater.*, 2019, **9**, 1901801.
91 K. Rokesh, M. Sakar and T.-O. Do, 2-(Aminomethyl pyridine)SbI_5: An emerging visible-light driven organic–inorganic hybrid perovskite for photoelectrochemical and photocatalytic applications, *Mater. Lett.*, 2019, **242**, 99–102.
92 Y. Guo, G. Liu, Z. Li, Y. Lou, J. Chen and Y. Zhao, Stable lead-free $(CH_3NH_3)_3Bi_2I_9$ perovskite for photocatalytic hydrogen generation, *ACS Sustain. Chem. Eng.*, 2019, **7**, 15080–15085.
93 G. Q. Chen, P. Wang, Y. Q. Wu, Q. Q. Zhang, Q. Wu, Z. Y. Wang, Z. K. Zheng, Y. Y. Liu, Y. Dai and B. B. Huang, Lead-free halide perovskite $Cs_3Bi_{2x}Sb_{2-2x}I_9$($x \approx 0.3$) possessing the photocatalytic activity for hydrogen evolution comparable to that of $(CH_3NH_3)PbI_3$, *Adv. Mater.*, 2020, **32**, 2001344.
94 F. Liu, M. Wang, X. Liu, B. Wang, C. Li, C. Liu, Z. Lin and F. Huang, A rapid and robust light-and-solution-triggered in situ crafting of organic passivating membrane over metal halide perovskites for markedly improved stability and photocatalysis, *Nano Lett.*, 2021, **21**, 1643–1650.
95 H. Yin, J. Chen, P. Guan, D. Zheng, Q. Kong, S. Yang, P. Zhou, B. Yang, T. Pullerits and K. Han, Controlling photoluminescence and photocatalysis activities in lead-free $Cs_2Pt_xSn_{1-x}Cl_6$ perovskites *via* ion substitution, *Angew. Chem., Int. Ed.*, 2021, **60**, 22693–22699.
96 H. Zhao, K. Chordiya, P. Leukkunen, A. Popov, M. Upadhyay Kahaly, K. Kordas and S. Ojala, Dimethylammonium iodide stabilized bismuth halide perovskite photocatalyst for hydrogen evolution, *Nano Res.*, 2021, **14**, 1116–1125.

97 Z. He, Q. Tang, X. Liu, X. Yan, K. Li and D. Yue, Lead-free $Cs_2AgBiBr_6$ perovskite with enriched surface defects for efficient photocatalytic hydrogen evolution, *Energy Fuels*, 2021, **35**, 15005–15009.

98 P. Zhou, H. Chen, Y. G. Chao, Q. H. Zhang, W. Y. Zhang, F. Lv, L. Gu, Q. Zhao, N. Wang, J. S. Wang and S. J. Guo, Single-atom Pt-I3 sites on all-inorganic Cs2SnI6 perovskite for efficient photocatalytic hydrogen production, *Nat. Commun.*, 2021, **12**, 4412.

99 Y. Q. Wu, Q. Wu, Q. Q. Zhang, Z. Z. Lou, K. F. Liu, Y. D. Ma, Z. Y. Wang, Z. K. Zheng, H. F. Cheng, Y. Y. Liu, Y. Dai, B. B. A. Huang and P. Wang, An organometal halide perovskite supported Pt single-atom photocatalyst for H_2 evolution, *Energy Environ. Sci.*, 2022, **15**, 1271–1281.

100 Y. Q. Tang, C. H. Mak, C. Wang, Y. Fu, F. F. Li, G. H. Jia, C. W. Hsieh, H. H. Shen, J. C. Colmenares, H. S. Song, M. J. Yuan, Y. Chen and H. Y. Hsu, Bandgap funneling in bismuth-based hybrid perovskite photocatalyst with efficient visible-light-driven hydrogen evolution, *Small Methods*, 2022, **6**, 2200326.

101 Y. L. Ji, M. Y. She, X. Bai, E. Z. Liu, W. H. Xue, Z. Zhang, K. R. Wan, P. Liu, S. Y. Zhang and J. L. Li, In-depth understanding of the effect of halogen-induced stable 2D bismuth-based perovskites for photocatalytic hydrogen evolution activity, *Adv. Funct. Mater.*, 2022, **32**, 2201721.

102 C. X. Bao, J. Yang, S. Bai, W. D. Xu, Z. B. Yan, Q. Y. Xu, J. M. Liu, W. J. Zhang and F. Gao, High performance and stable all-inorganic metal halide perovskite-based photodetectors for optical communication applications, *Adv. Mater.*, 2018, **30**, 1803422.

103 C. Liu, Y. Yang, O. A. Syzgantseva, Y. Ding, M. A. Syzgantseva, X. F. Zhang, A. M. Asiri, S. Y. Dai and M. K. Nazeeruddin, α-$CsPbI_3$ bilayers *via* one-step deposition for efficient and stable all-inorganic perovskite solar cells, *Adv. Mater.*, 2020, **32**, 2002632.

104 A. A. Zhumekenov, M. I. Saidaminov, M. A. Haque, E. Alarousu, S. P. Sarmah, B. Murali, I. Dursun, X.-H. Miao, A. L. Abdelhady, T. Wu, O. F. Mohammed and O. M. Bakr, Formamidinium lead halide perovskite crystals with unprecedented long carrier dynamics and diffusion length, *ACS Energy Lett.*, 2016, **1**, 32–37.

105 B.-W. Park, B. Philippe, X. Zhang, H. Rensmo, G. Boschloo and E. M. J. Johansson, Bismuth based hybrid perovskites $A_3Bi_2I_9$ (A: Methylammonium or cesium) for solar cell application, *Adv. Mater.*, 2015, **27**, 6806–6813.

106 W. Zhang, M. Hong and J. Luo, Halide double perovskite ferroelectrics, *Angew. Chem., Int. Ed.*, 2020, **59**, 9305–9308.

107 F. Jiang, D. Yang, Y. Jiang, T. Liu, X. Zhao, Y. Ming, B. Luo, F. Qin, J. Fan, H. Han, L. Zhang and Y. Zhou, Chlorine-incorporation-induced formation of the layered phase for antimony-based lead-Free perovskite solar cells, *J. Am. Chem. Soc.*, 2018, **140**, 1019–1027.

108 M. Liu, Y. Chen, J. Su, J. Shi, X. Wang and L. Guo, Photocatalytic hydrogen production using twinned nanocrystals and an unanchored NiS_x co-catalyst, *Nat. Energy*, 2016, **1**, 16151.

109 Y. Yang, C. Liu, M. L. Cai, Y. J. Liao, Y. Ding, S. Ma, X. P. Liu, M. Guli, S. Y. Dai and M. K. Nazeeruddin, Dimension-controlled growth of antimony-based perovskite-like halides for lead-free and semitransparent photovoltaics, *ACS Appl. Mater. Interfaces*, 2020, **12**, 17062–17069.

110 X. Meng, S. Wang, C. Zhang, C. Dong, R. Li, B. Li, Q. Wang and Y. Ding, Boosting hydrogen evolution performance of a CdS-based photocatalyst: In situ transition from type I to type II heterojunction during photocatalysis, *ACS Catal.*, 2022, **12**, 10115–10126.

111 H. Cai, B. Wang, L. Xiong, J. Bi, L. Yuan, G. Yang and S. Yang, Orienting the charge transfer path of type-II heterojunction for photocatalytic hydrogen evolution, *Appl. Catal., B*, 2019, **256**, 117853.

112 B.-J. Ng, L. K. Putri, X. Y. Kong, Y. W. Teh, P. Pasbakhsh and S.-P. Chai, Z-Scheme photocatalytic systems for solar water splitting, *Adv. Sci.*, 2020, **7**, 1903171.

113 X. Wang, H. Wang, H. Zhang, W. Yu, X. Wang, Y. Zhao, X. Zong and C. Li, Dynamic interaction between methylammonium lead iodide and TiO_2 nanocrystals leads to enhanced photocatalytic H_2 evolution from HI splitting, *ACS Energy Lett.*, 2018, **3**, 1159–1164.

114 M. V. Pavliuk, M. Abdellah and J. Sá, Hydrogen evolution with $CsPbBr_3$ perovskite nanocrystals under visible light in solution, *Mater. Today Commun.*, 2018, **16**, 90–96.

115 Y. Wu, P. Wang, X. Zhu, Q. Zhang, Z. Wang, Y. Liu, G. Zou, Y. Dai, M.-H. Whangbo and B. Huang, Composite of $CH_3NH_3PbI_3$ with reduced graphene oxide as a highly efficient and stable visible-light photocatalyst for hydrogen evolution in aqueous HI solution, *Adv. Mater.*, 2018, **30**, 1704342.

116 R. Li, X. Li, J. Wu, X. Lv, Y.-Z. Zheng, Z. Zhao, X. Ding, X. Tao and J.-F. Chen, Few-layer black phosphorus-on-$MAPbI_3$ for superb visible-light photocatalytic hydrogen evolution from HI splitting, *Appl. Catal., B*, 2019, **259**, 118075.

117 Z. Zhao, J. Wu, Y.-Z. Zheng, N. Li, X. Li and X. Tao, Ni_3C-decorated $MAPbI_3$ as visible-light photocatalyst for H_2 evolution from HI splitting, *ACS Catal.*, 2019, **9**, 8144–8152.

118 H. Wang, X. Wang, R. Chen, H. Zhang, X. Wang, J. Wang, J. Zhang, L. Mu, K. Wu, F. Fan, X. Zong and C. Li, Promoting photocatalytic H_2 evolution on organic–inorganic hybrid perovskite nanocrystals by simultaneous dual-charge transportation modulation, *ACS Energy Lett.*, 2019, **4**, 40–47.

119 T. Wang, D. Yue, X. Li and Y. Zhao, Lead-free double perovskite $Cs_2AgBiBr_6$/RGO composite for efficient visible light photocatalytic H_2 evolution, *Appl. Catal., B*, 2020, **268**, 118399.

120 B. M. Bresolin, P. Sgarbossa, D. W. Bahnemann and M. Sillanpaa, $Cs_3Bi_2I_9$/g-C_3N_4 as a new binary photocatalyst for efficient visible-light photocatalytic processes, *Sep. Purif. Technol.*, 2020, **251**, 117320.

121 G. N. Liu, R. Y. Zhao, B. Xu, Y. Sun, X. M. Jiang, X. Hu and C. Li, Design, synthesis, and photocatalytic application of moisture-stable hybrid lead-free perovskite, *ACS Appl. Mater. Interfaces*, 2020, **12**, 54694–54702.

122 Y. Zhao, Q. Zeng, Y. Yu, T. Feng, Y. Zhao, Z. Wang, Y. Li, C. Liu, J. Liu, H. Wei, S. Zhu, Z. Kang, H. Zhang and B. Yang, Enhanced charge separation and photocatalytic hydrogen evolution in carbonized-polymer-dot-coupled lead halide perovskites, *Mater. Horizons*, 2020, **7**, 2719–2725.

123 F. Wang, X. Liu, Z. Zhang and S. Min, A noble-metal-free MoS_2 nanosheet-coupled $MAPbI_3$ photocatalyst for efficient and stable visible-light-driven hydrogen evolution, *Chem. Commun.*, 2020, **56**, 3281–3284.

124 Y. Tang, C. H. Mak, R. Liu, Z. Wang, L. Ji, H. Song, C. Tan, F. Barrière and H. Y. Hsu, In situ formation of bismuth-based perovskite heterostructures for high-performance cocatalyst-free photocatalytic hydrogen evolution, *Adv. Funct. Mater.*, 2020, **30**, 2006919.

125 C. Cai, Y. Teng, J. H. Wu, J. Y. Li, H. Y. Chen, J. H. Chen and D. B. Kuang, In situ photosynthesis of an $MAPbI_3$/CoP hybrid heterojunction for efficient photocatalytic hydrogen evolution, *Adv. Funct. Mater.*, 2020, **30**, 2001478.

126 X. Zhao, S. Chen, H. Yin, S. Jiang, K. Zhao, J. Kang, P. F. Liu, L. Jiang, Z. Zhu, D. Cui, P. Liu, X. Han, H. G. Yang and H. Zhao, Perovskite microcrystals with intercalated monolayer MoS_2 nanosheets as advanced photocatalyst for solar-powered hydrogen generation, *Matter*, 2020, **3**, 935–949.

127 Y. Zhang, J. Shi, X. Ding, J. Wu, Y.-Z. Zheng and X. Tao, Stable mixed-organic-cation perovskite $MA_{1-x}FA_xPbI_3$ integrated with MoS_2 for enhanced visible-light photocatalytic H_2 evolution, *Ind. Eng. Chem. Res.*, 2020, **59**, 20667–20675.

128 L. Romani, A. Speltini, F. Ambrosio, E. Mosconi, A. Profumo, M. Marelli, S. Margadonna, A. Milella, F. Fracassi, A. Listorti, F. De Angelis and L. Malavasi, Water-stable $DMASnBr_3$ lead-free perovskite for effective solar-driven photocatalysis, *Angew. Chem., Int. Ed.*, 2021, **60**, 3611–3618.

129 L. Jiang, Y. Guo, S. Qi, K. Zhang, J. Chen, Y. Lou and Y. Zhao, Amorphous NiCoB-coupled $MAPbI_3$ for efficient photocatalytic hydrogen evolution, *Dalton Trans.*, 2021, **50**, 17960–17966.

130 L. Romani, A. Speltini, C. N. Dibenedetto, A. Listorti, F. Ambrosio, E. Mosconi, A. Simbula, M. Saba, A. Profumo, P. Quadrelli, F. De Angelis and L. Malavasi, Experimental strategy and mechanistic view to boost the photocatalytic activity of $Cs_3Bi_2Br_9$ lead-free perovskite derivative by g-C_3N_4 composite engineering, *Adv. Funct. Mater.*, 2021, **31**, 2104428.

131 W. Guan, Y. Li, Q. Zhong, H. Liu, J. Chen, H. Hu, K. Lv, J. Gong, Y. Xu, Z. Kang, M. Cao and Q. Zhang, Fabricating $MAPbI_3$/MoS_2 composites for improved photocatalytic performance, *Nano Lett.*, 2021, **21**, 597–604.

132 Y. Jiang, K. Li, X. Wu, M. Zhu, H. Zhang, K. Zhang, Y. Wang, K. P. Loh, Y. Shi and Q. H. Xu, In situ synthesis of lead-free halide perovskite $Cs_2AgBiBr_6$ supported on nitrogen-doped carbon for efficient hydrogen evolution in aqueous HBr solution, *ACS Appl. Mater. Interfaces*, 2021, **13**, 10037–10046.

133 W. B. Li, F. Wang, Z. G. Zhang, X. H. Ma and S. X. Min, Coupling of $MAPbI_3$ microcrystals with conductive polyaniline for efficient visible-light-driven H_2 evolution, *Sustain, Energy Fuels*, 2021, **6**, 76–80.

134 Y. Zhang, Z. Sun, Z. Wang, Y. Zang and X. Tao, Efficient and long-term photocatalytic H_2 evolution stability enabled by $Cs_2AgBiBr_6$/MoS_2 in aqueous HBr solution, *Int. J. Hydrogen Energy*, 2022, **47**, 8829–8840.

135 S. Feng, S. Ning, L. Wang, J. Zhao, J. Ou, Z. Wu, S. Luo, Z. Lin, K. Yan, C. Wu and Y. Xu, Modifying $CsPbX_3$ (X = Cl, Br, I) with a zeolitic imidazolate framework through mechanical milling for aqueous photocatalytic H_2 evolution, *ACS Appl. Energy Mater.*, 2022, **5**, 6248–6255.

136 K. Song, J. Gou, L. Yang and C. Zeng, Environmentally stable mesoporous g-C_3N_4 modified lead-free double perovskite $Cs_2AgBiBr_6$ for highly efficient photocatalytic hydrogen evolution, *Catal. Lett.*, 2023, **153**, 534–543.

137 Q. Huang, Y. M. Guo, J. X. Chen, Y. B. Lou and Y. X. Zhao, NiCoP modified lead-free double perovskite $Cs_2AgBiBr_6$ for efficient photocatalytic hydrogen generation, *New J. Chem.*, 2022, **46**, 7395–7402.

138 T. Chen, M. Li, L. Shen, M. B. J. Roeffaers, B. Weng, H. Zhu, Z. Chen, D. Yu, X. Pan, M. Q. Yang and Q. Qian, Photocatalytic anaerobic oxidation of aromatic alcohols coupled with H_2 production over $CsPbBr_3$/GO-Pt catalysts, *Front. Chem.*, 2022, **10**, 833784.

139 Q. Xu, L. Zhang, B. Cheng, J. Fan and J. Yu, S-scheme heterojunction photocatalyst, *Chem*, 2020, **6**, 1543–1559.

140 H. Li, S. Tao, S. Wan, G. Qiu, Q. Long, J. Yu and S. Cao, S-scheme heterojunction of ZnCdS nanospheres and dibenzothiophene modified graphite carbon nitride for enhanced H_2 production, *Chin. J. Catal.*, 2023, **46**, 167–176.

141 C. Cheng, J. Zhang, B. Zhu, G. Liang, L. Zhang and J. Yu, Verifying the charge-transfer mechanism in S-scheme heterojunctions using femtosecond transient absorption spectroscopy, *Angew. Chem., Int. Ed.*, 2023, **62**, e202218688.

142 F. Zhao, Y. L. Law, N. Zhang, X. Wang, W. Wu, Z. Luo and Y. Wang, Constructing spatially separated cage-like Z-scheme heterojunction photocatalyst for enhancing photocatalytic H_2 evolution, *Small*, 2023, **19**, 2208266.

143 Z. Long, X. Yang, X. Huo, X. Li, Q. Qi, X. Bian, Q. Wang, F. Yang, W. Yu and L. Jiang, Bioinspired Z-scheme In_2O_3/C_3N_4 heterojunctions with tunable nanorod lengths for enhanced photocatalytic hydrogen evolution, *Chem. Eng. J.*, 2023, **461**, 141893.

144 H. Zhou, Q. Chen, G. Li, S. Luo, T.-B. Song, H.-S. Duan, Z. Hong, J. You, Y. Liu and Y. Yang, Interface engineering of highly efficient perovskite solar cells, *Science*, 2014, **345**, 542–546.

145 N. J. Jeon, H. G. Lee, Y. C. Kim, J. Seo, J. H. Noh, J. Lee and S. I. Seok, *o*-Methoxy substituents in spiro-OMeTAD for efficient inorganic–organic hybrid perovskite solar cells, *J. Am. Chem. Soc.*, 2014, **136**, 7837–7840.

146 M. B. Zakaria, C. Li, Q. Ji, B. Jiang, S. Tominaka, Y. Ide, J. P. Hill, K. Ariga and Y. Yamauchi, Self-construction from 2D to 3D: One-pot layer-by-layer assembly of graphene

oxide sheets held together by coordination polymers, *Angew. Chem., Int. Ed.*, 2016, **55**, 8426–8430.

147 H. Zhang, Z. Luo, Y. Liu and Y. Jiang, Noble-metal-free Ni_3C as co-catalyst on $LaNiO_3$ with enhanced photocatalytic activity, *Appl. Catal., B*, 2020, **277**, 119166.

148 R. C. Shen, K. L. He, A. P. Zhang, N. Li, Y. H. Ng, P. Zhang, J. Hu and X. Li, In-situ construction of metallic Ni_3C@Ni core-shell cocatalysts over g-C_3N_4 nanosheets for shell-thickness-dependent photocatalytic H_2 production, *Appl. Catal., B*, 2021, **291**, 120104.

149 M. Sun, H. Liu, J. Qu and J. Li, Earth-Rich transition metal phosphide for energy conversion and storage, *Adv. Energy Mater.*, 2016, **6**, 1600087.

150 S. Cao, C.-J. Wang, W.-F. Fu and Y. Chen, Metal phosphides as co-catalysts for photocatalytic and photoelectrocatalytic water splitting, *ChemSusChem*, 2017, **10**, 4306–4323.

151 F. Zhang, J. Zhang, J. Li, X. Jin, Y. Li, M. Wu, X. Kang, T. Hu, X. Wang, W. Ren and G. Zhang, Modulating charge transfer dynamics for g-C_3N_4 through a dimension and interface engineered transition metal phosphide co-catalyst for efficient visible-light photocatalytic hydrogen generation, *J. Mater. Chem. A*, 2019, **7**, 6939–6945.

152 Y. Liu, X. Li, Q. Zhang, W. Li, Y. Xie, H. Liu, L. Shang, Z. Liu, Z. Chen, L. Gu, Z. Tang, T. Zhang and S. Lu, A general route to prepare low-ruthenium-content bimetallic electrocatalysts for pH-universal hydrogen evolution reaction by using carbon quantum dots, *Angew. Chem., Int. Ed.*, 2020, **59**, 1718–1726.

153 M. Han, C. Y. Kang, Z. X. Qu, S. J. Zhu and B. Yang, Surface molecule induced effective light absorption and charge transfer for H_2 production photocatalysis in a carbonized polymer dots-carbon nitride system, *Appl. Catal., B*, 2022, **305**, 121064.

154 Z. H. Pan, T. Hisatomi, Q. Wang, S. S. Chen, A. Iwase, M. Nakabayashi, N. Shibata, T. Takata, M. Katayama, T. Minegishi, A. Kudo and K. Domen, Photoreduced graphene oxide as a conductive binder to improve the water splitting activity of photocatalyst sheets, *Adv. Funct. Mater.*, 2016, **26**, 7011–7019.

155 H. L. Tan, H. A. Tahini, X. Wen, R. J. Wong, X. Tan, A. Iwase, A. Kudo, R. Amal, S. C. Smith and Y. H. Ng, Interfacing $BiVO_4$ with reduced graphene oxide for enhanced photoactivity: A tale of facet dependence of electron shuttling, *Small*, 2016, **12**, 5295–5302.

156 D. Mateo, I. Esteve-Adell, J. Albero, J. F. S. Royo, A. Primo and H. Garcia, 111 oriented gold nanoplatelets on multilayer graphene as visible light photocatalyst for overall water splitting, *Nat. Commun.*, 2016, **7**, 11819.

157 Y. Li, Z. Yin, G. Ji, Z. Liang, Y. Xue, Y. Guo, J. Tian, X. Wang and H. Cui, 2D/2D/2D heterojunction of Ti_3C_2 MXene/MoS_2 nanosheets/TiO_2 nanosheets with exposed (001) facets toward enhanced photocatalytic hydrogen production activity, *Appl. Catal., B*, 2019, **246**, 12–20.

158 B. J. Sun, W. Zhou, H. Z. Li, L. P. Ren, P. Z. Qiao, W. Li and H. G. Fu, Synthesis of particulate hierarchical tandem heterojunctions toward optimized photocatalytic hydrogen production, *Adv. Mater.*, 2018, **30**, 1804282.

159 C. B. Bie, B. C. Zhu, L. X. Wang, H. G. Yu, C. H. Jiang, T. Chen and J. G. Yu, A bifunctional CdS/MoO_2/MoS_2 catalyst enhances photocatalytic H_2 evolution and pyruvic acid synthesis, *Angew. Chem., Int. Ed.*, 2022, **61**, e2022120.

160 Y. Lei, M. Yang, J. Hou, F. Wang, E. Cui, C. Kong and S. Min, Thiomolybdate $[Mo_3S_{13}]^{2-}$ nanocluster: a molecular mimic of MoS_2 active sites for highly efficient photocatalytic hydrogen evolution, *Chem. Commun.*, 2018, **54**, 603–606.

161 J. Shi, R. Tong, X. Zhou, Y. Gong, Z. Zhang, Q. Ji, Y. Zhang, Q. Fang, L. Gu, X. Wang, Z. Liu and Y. Zhang, Temperature-mediated selective growth of MoS_2/WS_2 and WS_2/MoS_2 vertical stacks on Au foils for direct photocatalytic applications, *Adv. Mater.*, 2016, **28**, 10664–10672.

162 H. He, J. Lin, W. Fu, X. Wang, H. Wang, Q. Zeng, Q. Gu, Y. Li, C. Yan, B. K. Tay, C. Xue, X. Hu, S. T. Pantelides, W. Zhou and Z. Liu, MoS_2/TiO_2 edge-on heterostructure for efficient photocatalytic hydrogen evolution, *Adv. Energy Mater.*, 2016, **6**, 1600464.

163 T. F. Jaramillo, K. P. Jørgensen, J. Bonde, J. H. Nielsen, S. Horch and I. Chorkendorff, Identification of active edge sites for electrochemical H_2 evolution from MoS_2 nanocatalysts, *Science*, 2007, **317**, 100–102.

164 H. I. Karunadasa, E. Montalvo, Y. Sun, M. Majda, J. R. Long and C. J. Chang, A molecular MoS_2 edge site mimic for catalytic hydrogen generation, *Science*, 2012, **335**, 698–702.

165 J. S. Cai, J. Y. Huang, S. C. Wang, J. Iocozzia, Z. T. Sun, J. Y. Sun, Y. K. Yang, Y. K. Lai and Z. Q. Lin, Crafting mussel-inspired metal nanoparticle-decorated ultrathin graphitic carbon nitride for the degradation of chemical pollutants and production of chemical resources, *Adv. Mater.*, 2019, **31**, 1806314.

166 F. Xue, Y. T. Si, C. Cheng, W. L. Fu, X. Y. Chen, S. H. Shen, L. Z. Wang and M. C. Liu, Electron transfer *via* homogeneous phosphorus bridges enabling boosted photocatalytic generation of H_2 and H_2O_2 from pure water with stoichiometric ratio, *Nano Energy*, 2022, **103**, 107799.

167 F. Lin, S. Zhou, G. H. Wang, J. Wang, T. Y. Gao, Y. R. Su and C. P. Wong, Electrostatic self-assembly combined with microwave hydrothermal strategy: construction of 1D/1D carbon nanofibers/crystalline g-C_3N_4 heterojunction for boosting photocatalytic hydrogen production, *Nano Energy*, 2022, **99**, 107432.

168 Z. P. Wang, Z. L. Wang, X. D. Zhu, C. Z. Ai, Y. M. Zeng, W. Y. Shi, X. D. Zhang, H. R. Zhang, H. W. Si, J. Li, C. Z. Wang and S. W. Lin, Photodepositing CdS on the active cyano groups decorated g-C_3N_4 in Z-scheme manner promotes visible-light-driven hydrogen evolution, *Small*, 2021, **17**, 2102699.

169 H. Yu, L. Shang, T. Bian, R. Shi, G. I. N. Waterhouse, Y. Zhao, C. Zhou, L.-Z. Wu, C.-H. Tung and T. Zhang, Nitrogen-doped porous carbon nanosheets templated from g-C_3N_4 as metal-free electrocatalysts for efficient

oxygen reduction reaction, *Adv. Mater.*, 2016, **28**, 5080–5086.
170 Q. Zhang, S. Huang, J. Deng, D. T. Gangadharan, F. Yang, Z. Xu, G. Giorgi, M. Palummo, M. Chaker and D. Ma, Ice-assisted synthesis of black phosphorus nanosheets as a metal-free photocatalyst: 2D/2D heterostructure for broadband H_2 evolution, *Adv. Funct. Mater.*, 2019, **29**, 1902486.
171 M. Z. Rahman, C. W. Kwong, K. Davey and S. Z. Qiao, 2D phosphorene as a water splitting photocatalyst: fundamentals to applications, *Energy Environ. Sci.*, 2016, **9**, 709–728.
172 R. Yan, T. Ma, M. Cheng, X. Tao, Z. Yang, F. Ran, S. Li, B. Yin, C. Cheng and W. Yang, Metal–organic-framework-derived nanostructures as multifaceted electrodes in metal–sulfur batteries, *Adv. Mater.*, 2021, **33**, 2008784.
173 A. Dhakshinamoorthy, A. M. Asiri and H. Garcia, 2D Metal–organic frameworks as multifunctional materials in heterogeneous catalysis and electro/photocatalysis, *Adv. Mater.*, 2019, **31**, 1900617.
174 X. Tao, Y. Zhao, S. Wang, C. Li and R. Li, Recent advances and perspectives for solar-driven water splitting using particulate photocatalysts, *Chem. Soc. Rev.*, 2022, **51**, 3561–3608.
175 Y. Zhang and N.-G. Park, Quasi-two-dimensional perovskite solar cells with efficiency exceeding 22%, *ACS Energy Lett.*, 2022, **7**, 757–765.
176 G. Liao, C. Li, S.-Y. Liu, B. Fang and H. Yang, Z-scheme systems: From fundamental principles to characterization, synthesis, and photocatalytic fuel-conversion applications, *Phys. Rep.*, 2022, **983**, 1–41.
177 F. Bella, G. Griffini, J.-P. Correa-Baena, G. Saracco, M. Grätzel, A. Hagfeldt, S. Turri and C. Gerbaldi, Improving efficiency and stability of perovskite solar cells with photocurable fluoropolymers, *Science*, 2016, **354**, 203–206.
178 Y. Kim, H. Kim, S. Graham, A. Dyer and J. R. Reynolds, Durable polyisobutylene edge sealants for organic electronics and electrochemical devices, *Sol. Energy Mater. Sol. Cells*, 2012, **100**, 120–125.
179 J. Li, R. Xia, W. Qi, X. Zhou, J. Cheng, Y. Chen, G. Hou, Y. Ding, Y. Li, Y. Zhao and X. Zhang, Encapsulation of perovskite solar cells for enhanced stability: Structures, materials and characterization, *J. Power Sources*, 2021, **485**, 229313.
180 Z. Huang, J. Long, R. Dai, X. Hu, L. Le, X. Meng, L. Tan and Y. Chen, Ultra-flexible and waterproof perovskite photovoltaics for washable power source applications, *Chem. Commun.*, 2021, **57**, 6320–6323.
181 Q. Zhang, S. Liu, M. He, W. Zheng, Q. Wan, M. Liu, X. Liao, W. Zhan, C. Yuan, J. Liu, H. Xie, X. Guo, L. Kong and L. Li, Stable lead-free tin halide perovskite with operational stability $>$ 1200 h by suppressing Tin(II) oxidation, *Angew. Chem., Int. Ed.*, 2022, **61**, e202205463.
182 Z. Xiao, Z. Song and Y. Yan, From lead halide perovskites to lead-free metal halide perovskites and perovskite derivatives, *Adv. Mater.*, 2019, **31**, 1803792.